Geophysical Journal International

Geophys. J. Int. (2023) **232,** 1926–1943
Advance Access publication 2022 November 10
GJI Seismology

https://doi.org/10.1093/gji/ggac431

Parametric spectral inversion of seismic source, path and site parameters: application to northeast Italy

Laura Cataldi [1,2] Valerio Poggi,[2] Giovanni Costa,[1] Stefano Parolai[2] and Benjamin Edwards[3]

[1] *Department of Mathematics and Geosciences, SeisRaM group, University of Trieste, Via Weiss* 4, 34128 *Trieste, Italy. E-mail: lcataldi@ogs.it*
[2] *Istituto Nazionale di Oceanografia e di Geofisica Sperimentale, Via Treviso* 55, 33100 *Cussignacco, Udine, Italy*
[3] *Department of Earth, Ocean and Ecological Sciences, University of Liverpool, Jane Herdman Building,* 4 *Brownlow Street, Liverpool L693GP, UK*

Accepted 2022 November 7. Received 2022 October 21; in original form 2022 May 13

SUMMARY

Strong ground motion prediction is a fundamental topic in the field of engineering seismology, as it provides the input for seismic hazard studies as well as for vulnerability and risk assessment. The spectral modelling approach can provide a realistic representation of ground motion behaviour, possibly including its frequency variability, as the full ground motion spectrum is modelled analytically. In its parametric form, this approach requires a careful calibration of the model, starting from empirical observations and fitting the source, path and the site-specific response assuming a predefined physically constrained functional form. This study explores the use of spectral modelling for a study area in northeast Italy, at the border with Slovenia and Austria. It is based on the parametrization of seismic source and attenuation effects, and it also allows to estimate site effects, as a by-product. The main innovation with respect to standard spectral modelling is the inclusion of dedicated uncertainty estimators in the functional form. Parametric inversion of source and path attenuation is performed on a data set corresponding to 23 events recorded by 24 stations located within the target area. The modular inversion setup allows to properly include *a priori* constraints in the mathematical solution to reduce trade-off between variables. Spectral amplification at each site is defined with respect to the network average rock condition, and its frequency-dependent component is estimated from residual analysis after the inversion. Inverted source parameters are comparable with reference values for the region available from literature (with seismic moments between 10^{13} and 10^{15} N·m, and related stress drop values in the range $1.5 - 15.5$ MPa); the same is also true for average attenuation properties (e.g. apparent frequency-independent attenuation quality factor Q_0 of 1145). For a selection of stations with available characterization based on different methods, a preliminary comparison of site-specific response functions shows that both the frequency value and amplitude of the main amplification peaks are well recovered. These encouraging results open to the possibility of subsequently using the calibrated model for forward modelling purposes.

Key words: Fourier analysis; Waveform inversion; Site effects.

1 INTRODUCTION

Strong ground motion prediction is a fundamental topic in the field of engineering seismology, as it provides the input for seismic hazard studies as well as for vulnerability and therefore for risk assessment. In areas of low to moderate seismicity, such as the northeastern region of Italy, the lack of strong-motion records prevents the direct formulation of ground motion prediction equations valid for large magnitude events. The most common solutions are either the calibration of strong ground motion equations from other seismically active areas (e.g. Scherbaum *et al.* 2005; Cotton *et al.* 2006), or the extrapolation from weak-motion modelling by stochastic generation of synthetic accelerograms (e.g. Atkinson & Boore 1995; Boore 2003). In both cases, accurate information on attenuation and site-specific amplification due to subsurface geology (known as site response) is needed to correctly calibrate the models to the area of application. The aim of this study is to obtain a ground-motion spectral model for a study area in northeast Italy, a moderate seismicity region at the border with Slovenia and Austria. While providing local estimates for seismic source parameters,

attenuation and site effects, the implementation of such model is relevant for engineering-oriented applications such as earthquake scenario hazard analysis.

The Fourier amplitude spectrum (FAS) of ground motion can be expressed as a product of the source spectrum, frequency-dependent attenuation factors and the site response. The separation of source, path and site effects in terms of physical phenomena is a non-trivial and nonlinear problem, when source parameters are directly estimated through inversion (Scherbaum 1990; Poggi *et al.* 2011). Many studies based on this approach have been carried out using different methodologies. In particular, the problem represented by FAS modelling can be addressed either with a parametric (e.g. Salazar *et al.* 2007; Drouet *et al.* 2008; Edwards *et al.* 2008; Bora *et al.* 2017 for Europe; Zollo *et al.* 2014 for Italy) or non-parametric approach. The latter choice is generally applied in the form of GIT (Generalized Inversion Technique), a non-parametric method first introduced and applied by Andrews (1986) and Castro *et al.* (1990). It is usually based on a linear, two-step procedure, in which data are first corrected for attenuation and then solved for source and site parameters. There are many examples of estimation of regional seismological properties using GIT, such as Castro *et al.* (1997), Parolai *et al.* (2000, 2004), Bindi *et al.* (2006), Oth *et al.* (2008, 2011); Pacor *et al.* (2016) was specifically dedicated to the Italian case. Klin *et al.* (2021) recently conducted a thorough analysis focused on site amplification estimation through GIT for a large set of permanent stations in northeast Italy. Depending on the characteristics of the used data set, and especially on its distance coverage, GIT can provide good insight into the potential complexity of FAS factors and especially those describing attenuation, as it does not pre-define its functional form. On the other hand, in the standard form, independent *a priori* knowledge is applied *a posteriori* on the obtained results, rather than directly used to constrain the inversion. When such information is available and a predictive application is required, other methodologies are usually preferred to provide more engineering seismology-oriented results (e.g. Rietbrock *et al.* 2013; Bora *et al.* 2015). In this study the parametric approach was followed, which relies on fitting a parametric spectral model to observed data; this choice was also based on the limited data set coverage (cf. Section 3). This method iteratively explores the model space based on the partial derivatives of the amplitude spectrum with respect to each parameter, which are computed at each step. The best solution for the parameters is obtained by recursive minimization of the misfit calculated from observed and estimated data. The resulting parameter estimates can be applied into seismic input prediction for damage assessment and for subsequent use in extending the problem to the nonlinear case (e.g. Bommer *et al.* 2017). In particular, a set of parameters dedicated to the quantification of uncertainty was included with the goal of minimizing possible trade-offs between source, path and site parameters of the model and, at the same time, to provide a reliable uncertainty estimation to be used in forward stochastic simulation.

Parametric inversion was performed on instrumental data recorded in the tectonically active area of northeast Italy, which displays low to moderate seismicity with some long-recurring events of higher magnitude (Galadini *et al.* 2005). Previous spectral analyses available in literature for this area include Castro *et al.* (1996, 1997), Malagnini *et al.* (2002) and Franceschina *et al.* (2006), all mainly focused on attenuation and quality factors. The region is monitored by many seismic networks, both at regional, national and trans-national level. When individual national seismic bulletins are considered, the trans-frontier localization of the area could in principle limit the event coverage and thus the localization quality in the case of seismic events occurred near national borders. The preferred localization provided by the International Seismological Centre (ISC) web bulletin was thus adopted, as it results from a homogeneous revision of all available event localizations.

Frequency-dependent site amplification functions were estimated for a set of sites in the area of interest by performing residual analysis on the inversion output. The current site classification of most Italian national accelerometric stations is in the form of Eurocode-8 (EC8 2004) classes, mainly relying on geological and topographic maps and visual description of sites. Information on $v_{s_{30}}$ is often indirectly estimated, and sometimes totally missing. The results obtained in this study are in good agreement with available preliminary information and could be used for direct application into site-specific seismic hazard assessment (Michel *et al.* 2017), should further dedicated validation confirm it.

2 SEISMOTECTONIC SETTING OF NORTHEAST ITALY

The study region displays significant seismic activity and suffered from strong destructive historical earthquakes, mostly originated in the Veneto and Idrija regions. The main orographic feature is the eastern part of the Southalpine Chain, where the Southern Alps interact with the Dinaric mountain belt (Cuffaro *et al.* 2010). Fig. 1 shows the main seismogenic sources, as described by *Zonazione Sismogenetica—ZS9* seismic source model (Meletti & Valensise 2004), and the regional seismic activity for the period 1976–2017, as given by the reviewed ISC bulletin (International Seismological Centre 2020). Most events have low to moderate magnitude, with some higher magnitude exceptions like the 1976 Friuli (Italy) earthquake and the 1998 and 2004 Bovec-Krn (Slovenia) sequences. Associated hypocentral depths are usually shallow and below 20 km. The predominant faulting style for the Alpine area is the compressive one, whereas more strike-slip patterns appear by moving to the West in Veneto and Austria, and to the East in Slovenia (Bressan *et al.* 2003).

3 DATA SET

Northeast Italy regional seismic activity has been recorded both by national and local networks since the late 1970s, after the destructive sequence of the 1976 Friuli earthquake led to an increase in the monitoring coverage. Seismic stations are densely present in the Friuli Venezia Giulia area, with coverage also towards Veneto, Slovenia and Austria.

The target area was defined as a simple polygon encasing all the main regional seismogenic features and as many stations as possible (Fig. 2). It extends from the margin of the Veneto plain to the west to the Slovenian border to the east, and from the Venetian lagoon to the south to the Austrian border on the Alps chain to the north. A further buffer area was defined to be used as additional source for events only. This event buffer area forms an almost regular frame around the polygon delimiting the target area (9.8–16.3 ° E, 45.0–47.7 ° N), with limited extension to the south. This ensures the exclusion of events originated in the Po river plain, for which a characteristic enhancement of ground motion has been observed at distances between 90 and 150 km as an effect of the reflection of *S* waves at the Moho (Bragato *et al.* 2011; Sugan & Vuan 2014).

The event buffer area covers a trans-frontier region between three different countries. To ensure catalogue homogeneity, parametric information was taken from the preferred localization suggested

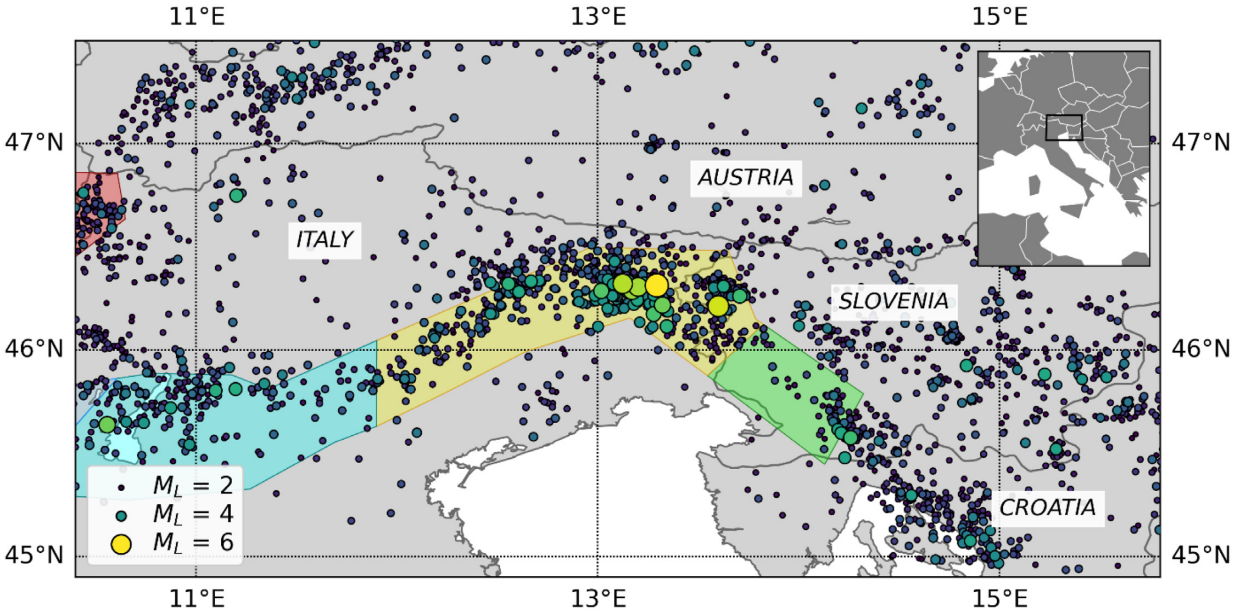

Figure 1. Seismicity of the study area in the period 1976–2017 (filled circles). The main seismogenic sources populating the area are also pictured in the form of *ZS9* seismogenic zones (filled polygons).

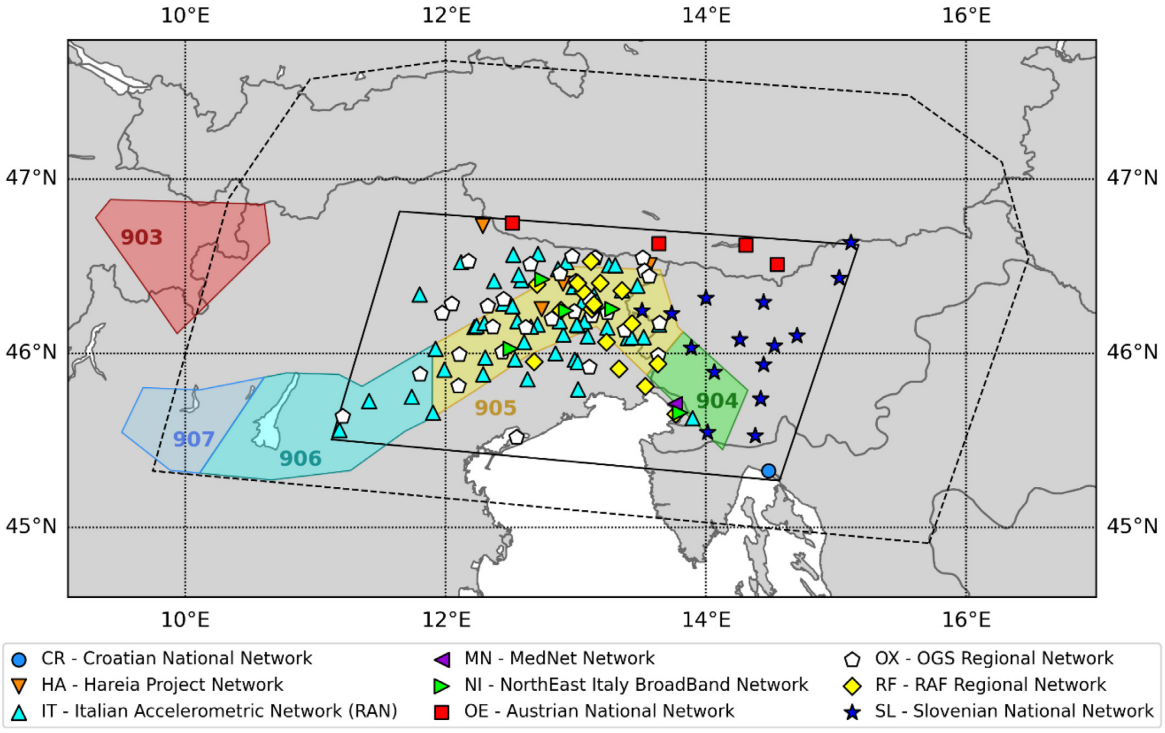

Figure 2. The case study area (solid black polygon) in northeast Italy. The outer dotted black polygon marks the corresponding buffer area. Filled polygons represent seismogenic zones as defined according to ZS9. Different markers indicate the location of recording stations belonging to different seismic networks in the area.

by the reviewed ISC bulletin, which results from expert revision of location solutions provided by different European agencies for events up to 2019. The search was limited to seismic events having occurred after 2009, when the seismic station coverage in the area started to increase significantly, together with the quality of the installed instruments. A constraint was imposed that information on the local magnitude (M_L) value of the event should be present, with $M_L \geq 2$ to limit the impact of noise.

4 INPUT DATA AND SPECTRA COMPUTATION

The initial selection of events taken from the ISC bulletin was matched with the available instrumental data recorded by stations inside the target area, with the condition of inclusion of only the highest quality data and metadata (i.e. instrumental correction factors). A conservative decision was made to use the revised waveform

database available from SeisRaM group at the University of Trieste, which relies on the trans-frontier European network CE3RN (Bragato *et al.* 2014) and gathers data collected from IT, NI, RF, SL, CR, AT and MN networks (cf. Fig. 2 or section on Data availability and resources for network definitions) in the time span 2012–2017. This choice ensures the homogeneity and accuracy of waveform data, seismometer calibration and response functions alike, and guarantees that response functions can be correctly deconvolved from the spectra (cf. Section 5.1).

Following the approach suggested by Edwards *et al.* (2008) to improve the stability of the results, some constraints were applied to the three-component accelerometric data set before use. Stations with less than five records related to the selected events were discarded, as well as recordings with no associated picks. If only one pick was recorded (either *P* or *S*), the other arrival time was estimated using a *P*:*S* velocity ratio of 1.73. The composition of the database ($M_L \leq 4.6$ and hypocentral distances over 10 km) ensured that criteria for the use of point source spectral models were met (Brune 1970, 1971; Boatwright 1978).

Instrumental data was pre-processed following a procedure modified from Gallo *et al.* (2014). It includes the automatic calculation of the usable frequency range between 0.1 and 50 Hz, based on signal-to-noise ratio (SNR). The pre-processing was used to determine the actual number of traces containing useful information related to the selected events. A 10-s noise window (prior to *P*-wave arrival) was extracted along with a full time-series signal window, with length corresponding to 5–95 per cent of the energy integral (maximum duration of 75 s) beginning at the *P*-wave onset. A maximum frequency range of 0.5–25 Hz was imposed to focus the inversion on the range of interest for site amplification effects, with the minimum requirement of SNR values greater than 2.8 over the bandwidth $2 - 10$ Hz. All traces are recorded by seismometers with sampling frequency above 100 Hz, usually at 200 Hz. The lower bound was selected based on the availability of the noise window, which was limited to 10 s , since most waveforms came from triggered recordings. As the lowermost frequency sampled by the noise window is around 0.1 Hz, this conservative choice ensured that at least a few cycles of each sampled frequency were contributing to the noise spectra, in order to avoid underestimation.

After pre-processing, the waveform database was matched with information from the selected event catalogue by using a recursive procedure. Events with less than five associated recordings were discarded, then only stations with at least five recorded events were kept, until both conditions were matched at the same time. After all selection criteria were applied, a total of 234 three-component records was available for use in the spectral inversion, corresponding to $N_i = 23$ events (Table 1) recorded by $N_j = 24$ stations (Table 2). This limitation in the selection operated on the wider pool of available events and stations guarantees to pick the highest quality, best-recorded events.

The selected data set is mainly composed of low and intermediate magnitude events, reflecting the characteristic seismicity for the area, with corresponding moderate hypocentral distances. Corresponding metadata are summarized in Fig. 3, together with the distribution of ray paths, stations and earthquake epicentres. All events have moderate magnitude in the range $2.3 \leq M_L \leq 4.5$, with hypocentral distances up to 204 km, thus we expect the signal to be dominated by S_n and L_g regional seismic phases. All events are shallow crustal events with focal depths below 20 km. The station $v_{s_{30}}$ values range from 256 to 1263 m s^{-1}, all inferred from topographic slope using the method by Wald & Allen (2007) (cf. ITACA, D'Amico *et al.* 2020). Most stations are on *EC8-A* class soil, as defined in Eurocode-8, with some exceptions belonging to classes *EC8-B* and *EC8-C*.

Velocity FAS were extracted after integrating and detrending each accelerometric record. A standard Konno Ohmachi smoothing with $b = 40$ (Konno & Ohmachi 1998), which is symmetric in log-space, was applied to reduce the level of high-frequency fluctuations in the spectra. Amplitudes were estimated on a set of 30 log-distributed frequency points in the range $0.5 - 25.0$ Hz. A Boolean array was associated to each spectrum, to mark which frequency points had acceptable SNR values and thus should be used for inversion and which had to be discarded. The effective amplitude (root-mean-square) of the horizontal components was computed in the Fourier domain. Fig. 4 provides a schematic representation of this procedure.

5 METHODOLOGY

5.1 FAS modelling

Parametric inversion requires an *a priori* assumption on the functional form of the spectral model to be used for the calculation of the loss function. In general, the velocity FAS of ground motion observed at a station j, originating from an earthquake i, for any frequency point k, can be represented as the product of a source (Ω), a propagation (D) and a site (S) term:

$$FAS_{ijk}\left(r_{ij},\ f_k\right) = 2\pi f_k\ \Omega_i\left(f_k\right)\ D_{ij}\left(r_{ij},\ f_k\right)\ S_j\left(f_k\right)\ I_j\left(f_k\right), \tag{1}$$

where r_{ij} is the hypocentral distance and f is the frequency. The actual parametrization of each term depends on the used data set and on the assumptions on source, site and path characteristics. Preliminary careful deconvolution of data with the seismograph response functions allows to set the instrument response term $I(f)$ equal to one.

The chosen logarithmic form of the corresponding parametric model used for inversion is described by:

$$\begin{aligned}\log \mathrm{FAS}_{ijk}\left(r_{ij},\ f_k\right) = {} & \log\left(2\pi f_k\right) + \log\left(\frac{\Theta_{\lambda\varphi} F \xi}{4\pi\rho v_s^3 R_0}\right) + \log M_{0i} \\ & - \log\left(1 + \left(\frac{f_k}{f_{ci}}\right)^2\right) + \log G\left(r_{ij},\ f_k\right) \\ & - \frac{\pi f_k r_{ij}}{v_s Q_0} + \log A_j - \pi f_k \kappa_{0j} + \varepsilon_i^{SO} + \varepsilon^P .\end{aligned} \tag{2}$$

This functional form is built from a standard spectral model with the addition of the uncertainty collector terms $\boldsymbol{\varepsilon^{SO}}$ and ε^P, which are related to source and propagation contributions respectively (cf. end of Sections 5.1 and 5.4). The source term is in the form of a simple far field Brune spectrum, with f_c being the source corner frequency. The quantities on which it depends are the seismic moment M_0, the average radiation pattern $\Theta_{\lambda\varphi}$ ($= 0.55$ for *S* waves at local distances; Boore & Boatwright 1984), the free surface amplification factor F ($= 2$ for normally incident *SH* waves and a good approximation for *SV*), the factor to account for the partition of total shear-wave energy into two horizontal components ξ ($= 1/\sqrt{2}$), the reference distance used for normalization $R_0 = 1$ km, the average density near the source ρ ($= 2800$ kg m^{-3}; Boore 1983, 2003) and the shear wave velocity in the proximity of the source v_S ($= 3500$ m s^{-1}, comparably with regional estimates; e.g. Gentile *et al.* 2000). As the database is composed of low magnitude events ($M_L \leq 4.6$), the far-field approximation holds even for shorter distances (Bora *et al.* 2017).

Any correct deconvolution of velocimetric data into physical parameters describing seismic energy propagation must deal with the

Table 1. Events used for spectral inversion.

Event	Date	Time	Latitude (° N)	Longitude (° E)	Depth (km)	M_L	Number of records
1	2012–06-09	02:04:57	46.1 759	12.4 661	12.8	4.40	14
2	2013–08-24	13:59:01	46.1 743	12.4 841	14.4	3.70	8
3	2013–09-06	15:01:35	46.3 661	12.8 309	9.8	3.00	6
4	2013–10-31	18:46:22	46.2 083	12.5 133	10.6	3.20	5
5	2014–04-22	08:58:28	45.6 467	14.2 267	16.1	4.50	17
6	2014–05-29	07:24:19	46.0 679	13.8 304	18.2	3.30	10
7	2015–01-30	00:45:50	46.3 818	13.1 038	15.0	4.20	15
8	2015–05-12	02:02:50	45.8 601	12.0 389	15.8	3.50	13
9	2015–05-15	05:35:46	45.8 522	12.0 489	16.7	3.60	10
10	2015–08-17	00:15:33	46.4 579	13.2 708	13.7	2.60	12
11	2015–08-18	20:10:02	45.8 601	11.9 049	14.8	3.70	9
12	2015–08-29	18:47:04	46.3 029	13.5 776	10.6	4.00	16
13	2015–11-01	07:52:33	45.8 689	15.5 325	6.0	4.40	5
14	2015–11-11	19:46:37	46.4 951	12.8 281	16.6	3.20	14
15	2015–11-11	21:20:31	46.5 143	12.8 651	12.5	2.70	8
16	2015–11-21	11:52:38	46.4 392	12.7 366	11.8	3.30	16
17	2015–12-08	15:05:01	46.3 486	12.6 223	10.4	3.40	13
18	2016–07-19	22:36:50	46.4 190	13.0 883	13.0	2.50	5
19	2016–08-10	02:38:05	46.3 926	12.9 490	13.4	2.90	13
20	2016–12-22	08:43:54	46.2 919	13.3 403	12.8	2.30	5
21	2017–02-09	08:14:08	45.8 017	11.1 616	15.4	3.70	7
22	2017–03-23	13:11:07	46.3 245	13.1 601	13.	3.00	9
23	2017–03-24	17:47:07	46.3 393	13.0 263	7.7	2.50	5

Table 2. Stations used for spectral inversion. All of them are high-quality broad-band accelerometric stations.

Name	Network	Latitude (° N)	Longitude (° E)	Altitude (m)	Soil classification	v_{s30} (m s^{-1})
AUP	IT	46.506	13.256	904	Rock (*EC8-A*)	954
AVS	IT	46.295	13.050	206	Rock (*EC8-A*)	256
CARC	RF	45.653	13.77	2	Soil (*EC8-C*)	309
CESC	RF	46.356	13.057	355	Soil (*EC8-B*)	735
CHF	IT	46.389	13.474	1160	Rock (*EC8-A*)	710
CMO	IT	46.094	13.521	605	Rock (*EC8-A*)	1008
DANT	IT	46.568	12.52	1453	Rock (*EC8-A*)	860
DST2	NI	45.659	13.801	86	Rock (*EC8-A*)	583
FDS	IT	46.451	12.563	1780	Rock (*EC8-A*)	1099
FLP	IT	46.027	11.923	294	Soil (*EC8-C*)	452
GEDE	RF	46.254	13.124	180	Soil (*EC8-B*)	344
GEPF	RF	46.275	13.138	255	Rock (*EC8-A*)	1119
GESC	RF	46.282	13.141	320	Soil (*EC8-C*)	786
GORI	RF	45.940	13.631	142	Soil (*EC8-B*)	400
MASA	RF	46.172	13.431	640	Rock (*EC8-A*)	777
MOGG	RF	46.405	13.188	387	Rock (*EC8-A*)	795
PAUL	RF	46.530	13.116	640	Rock (*EC8-A*)	558
POLC	NI	46.026	12.500	150	Soil (*EC8-B*)	495
PRAD	RF	46.248	12.887	520	Rock (*EC8-A*)	455
PURA	NI	46.425	12.742	1420	Rock (*EC8-A*)	607
RST	IT	46.363	13.354	604	Rock (*EC8-A*)	1263
SPP	IT	46.572	12.709	1318	Soil (*EC8-C*)	816
STOL	RF	46.360	13.354	570	Soil (*EC8-C*)	660
TLM2	IT	46.381	12.984	519	Soil (*EC8-B*)	497

issue of trade-offs between the parameters themselves. The most documented and significant one is the trade-off between the apparent attenuation quality factor Q and the source corner frequency (e.g. Scherbaum 1990). Such effect might lead to large errors if the inversion is left unconstrained, with the possible propagation of errors into any resulting predictive equation. For this reason, trusted independent information on the parameters taken from literature was used to constrain the inversion, and all the results will be relative to the model we assumed. The apparent geometrical spreading term $G(r_{ij}, f_k)$ was taken from the simplified form proposed by Malagnini *et al.* (2002), who obtained it from a wider data set in the same tectonic and geological setting. The simplified

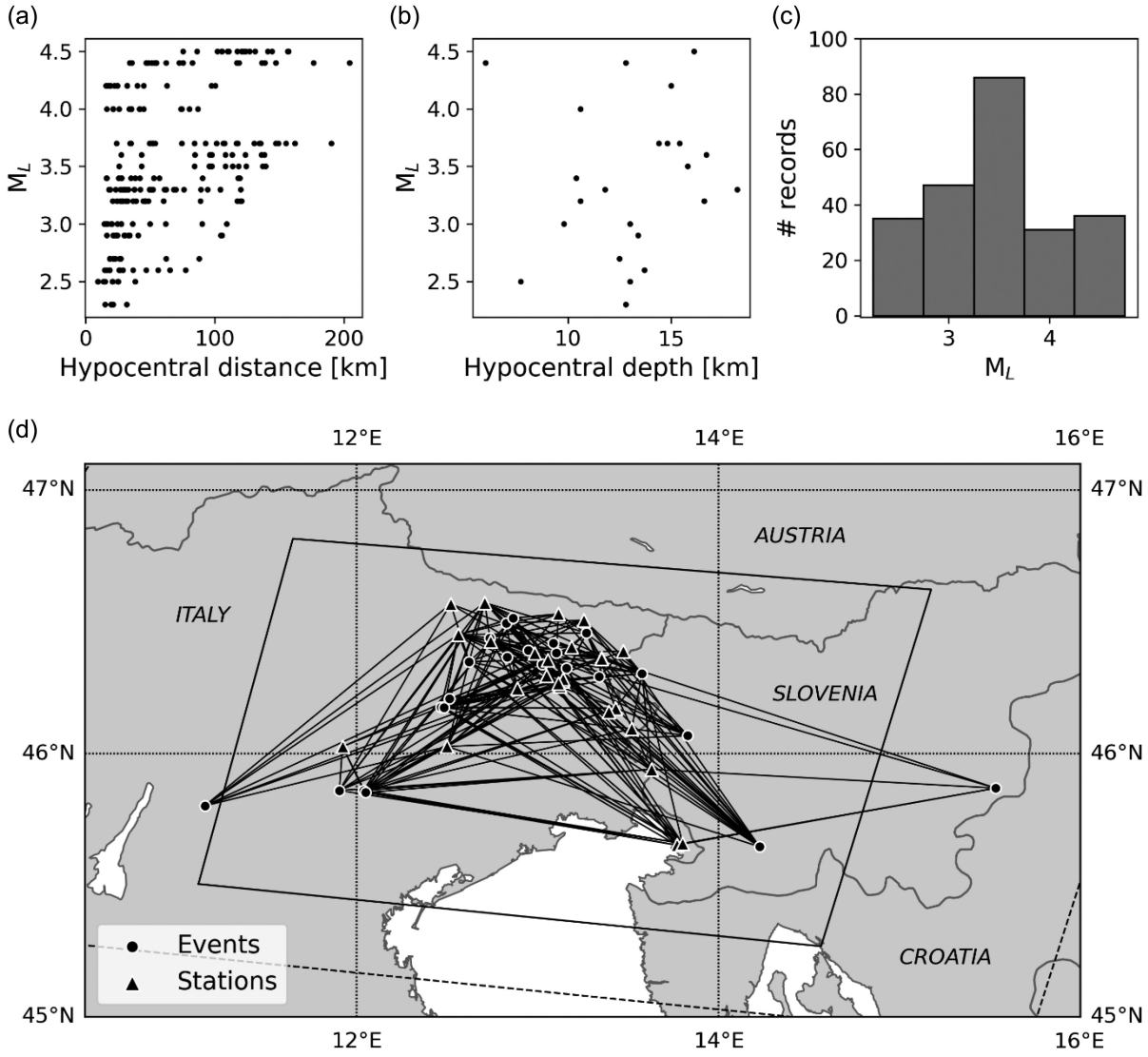

Figure 3. (a) Magnitude and hypocentral distance ranges, (b) hypocentral depths of the events, (c) distribution of events over the used magnitude range and (d) map of the target area with the used earthquakes (circles), stations (triangles) and rays (lines).

quality factor Q_0 and the site-related high-frequency spectral correction factor κ_0 are treated as frequency-independent. A_j is the frequency-independent correction factor relative to the chosen reference amplification profile. The frequency-dependent site response is left unmodelled and was retrieved through residual analysis (cf. Section 5.3).

This standard functional form was modified with the addition of a new, specific set of parameters ($\boldsymbol{\varepsilon}^{\boldsymbol{SO}}$ and ε^P) so that the algorithm could distinguish residual contributions tied to a specific event and to the overall path effects. In fact, the source term ε_i^{SO} gathers the uncertainty related to the implemented source parameters, namely $M_{0,i}$ and $f_{c,i}$. The uncertainty related to site components is not directly retrieved by inversion, but it instead obtained from the factorial residual analysis (cf. Section 5.4). This feature might be particularly helpful in the light of the possible bias introduced by trade-off between κ_{0j} and Q_0. It should be kept in mind that these uncertainty terms should not be read as errors related to a single parameter, but rather as collectors of the overall uncertainty residing in the correspondent parametric class, as in source, propagation or site. Other complementary approaches could be used for direct error estimation which were not applied in this work, such as *a posteriori* residual decomposition.

5.2 Parametric inversion

Parametric inversion was performed on the selected set of 234 velocity Fourier spectra to solve the linear system represented by eq. (1). A nonlinear quasi-Newton inversion method, which does not require the inversion of the Hessian matrix, was applied based on the initial *a priori* model. As a consequence of the aforementioned modelling choices, the parameter vector used in the inversion algorithm is in the form:

$$\boldsymbol{p} = \left[\left[\log M_{01}, \ldots, \log M_{0N_i}\right], \left[f_{c1}, \ldots, f_{cN_i}\right], Q_0, \left[\log A_1, \ldots, \log A_{N_j}\right], \left[\kappa_1, \ldots, \kappa_{N_j}\right], \left[\varepsilon_1^{SO}, \ldots, \varepsilon_{N_i}^{SO}\right], \varepsilon^P \right]. \quad (3)$$

It is composed of N_i terms for each of source spectra, corner frequency and source uncertainty vectors, one term for the attenuation factor and the propagation uncertainty term, and N_j terms for each of frequency-independent site amplification and site-related

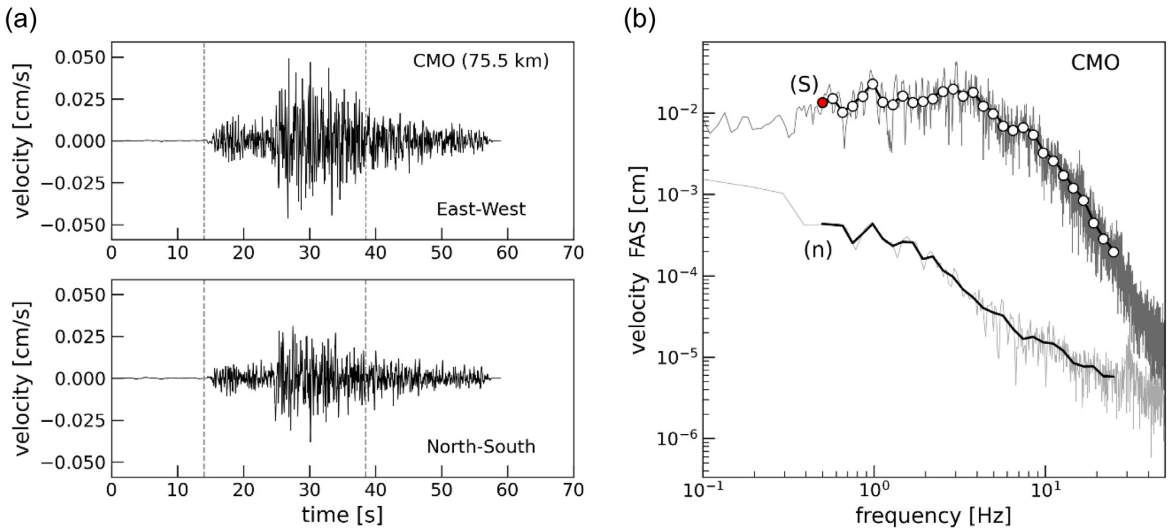

Figure 4. (a) Velocity traces for the east–west and north–south components of the 2014 April 22 earthquake (no. 5 in Table 1) at station CMO. Vertical dashed lines mark the time interval used for signal spectrum extraction. (b) Raw (grey lines) and smoothed (black lines) FAS of the velocity for signal (S) and noise (n) for the resultant horizontal component. The final corresponding spectrum used for inversion is represented as circle markers, with 30 frequency points lognormally distributed in the range 0.5–25 Hz. Each point has an assigned Boolean weight, equal to 1 if the point has sufficient SNR score (white circles) and equal to 0 otherwise (red circles).

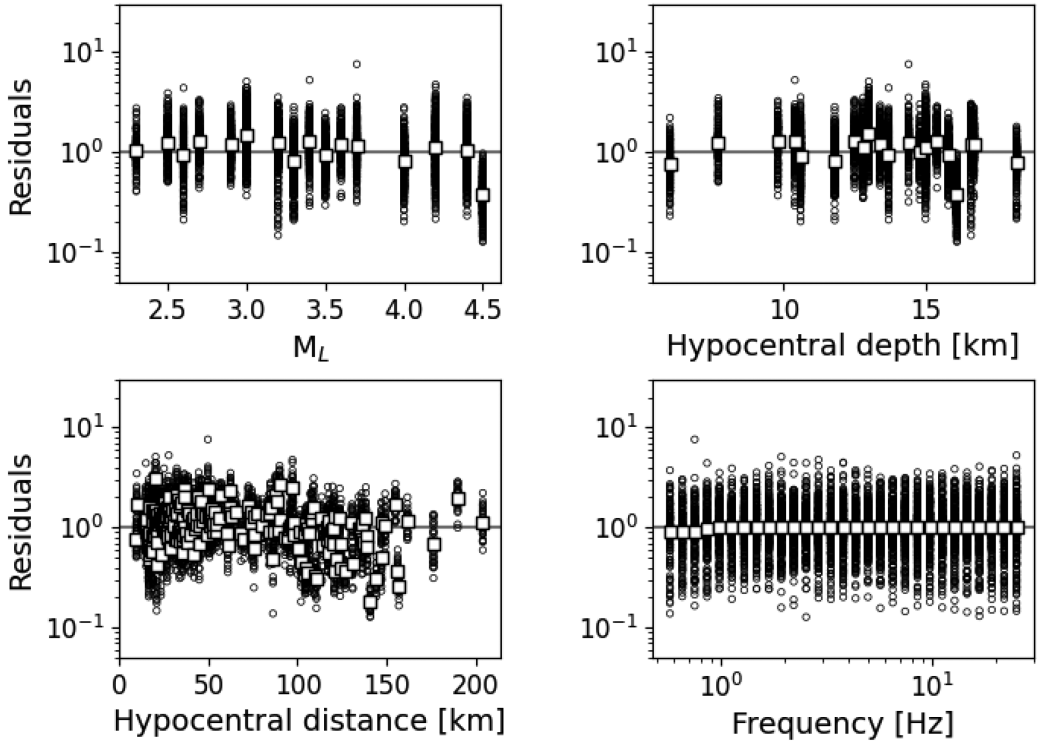

Figure 5. Overall residuals (data/model) with respect to a reference rock prediction plotted against hypocentral distance, source depth, local magnitude, and frequency. White squares indicate the log-mean residual at each hypocentral distance, source depth, local magnitude and frequency value. The residuals are plotted for the model obtained from the spectral inversion, plus the contribution of the frequency-dependent site response.

attenuation vectors.

A single-step inversion based on the Sequential Least-Squares Programming methodology (SLSQP; Kraft 1988) was performed, using a $\log - L_2$ loss function in the form:

$$LF = \sum_{i,j,k} \frac{\left[M_{ijk}\left(\log\left[\mathrm{FAS}^{o}_{ijk}\right] - \log\left[\mathrm{FAS}^{m}_{ijk}\right]\right)\right]^2}{N_{\mathrm{TOT}}}, \quad (4)$$

where M is the matrix of Boolean masks indicating which frequency points of each spectrum should be used for inversion, based on SNR. Superscripts o and m denote spectral values for the observed and the modelled data, respectively. Individual bounds were applied to each parameter to limit the search space to a physically meaningful region. A constraint was imposed on the constant amplitude correction terms A_j to define them with respect to a reference condition.

Ideally, the optimal reference would be a rock site for which no amplification is experienced, at any frequency. The choice for a reference site was thus narrowed to stations belonging to class A according to EC8 classification, and the inversion was constrained by assuming:

$$\sum_{EC8-A} \log\left(A_j\right) = 0, \tag{5}$$

so that parameter A_j is defined as the amplification relative to the network average rock-like (*EC8-A*) condition.

The chosen inversion strategy was converted into a python algorithm that recursively fits the observed FAS with respect to the chosen parametric model. At each iteration, the parameter set is perturbed using information from the Jacobian function and the corresponding loss function is calculated, until a threshold condition for minimization is met. Available *a priori* information on spectral parameters can be easily included in the minimization process, as the algorithm allows to properly constrain individual parameters.

Initial guesses for source parameters were obtained from the reference ISC bulletin. Seismic moment starting guesses (M_0^{IN}) were built from bulletin values of M_L by combining the scaling law by Hanks & Kanamori (1979):

$$\log_{10}\left(M_0^{IN}\right) = 1.5\ M_w + 9.05, \tag{6}$$

where M_w is the moment magnitude and M_0 is expressed in Nm, with the empirical relationship developed by Munafò *et al.* (2016) to correlate M_w and M_L for Italian earthquakes with small magnitudes (up to $M_w \sim 4$):

$$M_w = 0.67\ M_L + 1.15. \tag{7}$$

Brune's (1970, 1971) source model was used to calculate the initial guess for corner frequency values (f_c^{IN}) as a function of seismic moment and of the stress drop parameter $\Delta\sigma$:

$$f_c^{IN} = 0.4906\ v_s \left(\frac{\overline{\Delta\sigma}}{M_0^{IN}}\right)^{1/3}, \tag{8}$$

where $\overline{\Delta\sigma} = 0.73$ MPa is the average regional stress drop taken from literature (Franceschina *et al.* 2006). The corresponding upper and lower bounds for source parameters were obtained by propagating the magnitude uncertainty, conservatively set to 0.5. Bounds for the corner frequency values also took into consideration the estimated maximum span of stress drop values for the region ($0.1 - 5$ MPa; from Franceschina *et al.* 2006).

Starting values for propagation and site parameters were taken from region-specific literature. Given the adopted (frequency-independent) modelling choice, the actual parameter space provided to the algorithm was wide enough to cover different possibilities for the Q_0 value, from low ($Q_0 \sim 50$), to intermediate ($Q_0 \sim 500$), to high ($Q_0 \sim 1500$), with a starting value of $Q_0^{IN} = 260$ (from Malagnini *et al.* 2002). The average site-related attenuation value provided by Gentili & Franceschina (2011) was used to set $\kappa_0^{IN} = 0.037$ s for all stations, with boundaries allowing it to span in the range $0.01 - 1$ s to cover the many possible values reported in literature. As for the frequency-independent site amplification A^{IN} and the uncertainty terms, they were initially set to zero, with A^{IN} constrained as per eq. (5) so that the network average rock condition would be used as a reference. No bound was imposed on the uncertainty terms.

With this setting, the algorithm explores a broad model space, but still keeps the starting values in a realistic range around the attended real values so that the linearized inversion remains valid. Different starting configurations inside this model space were tested to check that the results of the inversion were not dependent on the starting model.

5.3 Residual analysis

Frequency-dependent response functions are left unmodelled by eq. (2) and can be constructed from the inversion residuals (Edwards *et al.* 2008; Edwards & Fäh 2013). The factorial residual of the inversion, given by:

$$\vartheta_{ij}\ (f_k) = \frac{\mathrm{FAS}_{ijk}^{o}}{\mathrm{FAS}_{ijk}^{m}}, \tag{9}$$

is used to reconstruct the frequency-dependent site functions by taking its log-space geometric mean at each discrete frequency f_k over all events ($i = 1, \ldots, N_i$), at each station j (e.g. Scherbaum 1990; Edwards *et al.* 2008):

$$\log\left(a_j\left(f_k\right)\right) = \frac{1}{N_i}\left\{\sum_{i=1}^{N_i} \log\left(\vartheta_{ij}\left(f_k\right)\right)\right\}. \tag{10}$$

The total site response functions (SRF) can be obtained by combining these frequency-dependent functions with the constant amplitude correction A and the κ_0 at the site:

$$\mathrm{SRF}_j\left(f_k\right) = A_j\ a_j\left(f_k\right) e^{-\pi f_k \kappa_{0j}}. \tag{11}$$

These SRFs are defined based on the inversion residuals and therefore should be interpreted carefully. The algorithm cannot distinguish between actual residuals to the model coming from the frequency-dependent amplification and those coming from noise and instrument calibration errors.

For this reason, careful data processing is needed to ensure that instrument effects at least are correctly subtracted. In fact, before proceeding with the analysis of results and with the extraction of site functions, the residuals were checked to make sure that no evident trend or trade-off emerged with respect to different possible quantities (magnitude, hypocentral distance, hypocentral depth and frequency). The residuals are calculated as model/data, where the model is already corrected for the frequency-dependent response function, and are plotted in Fig. 5. There is no evident dependency of the residuals on any considered quantity.

5.4 Uncertainty estimation

Parameters $\boldsymbol{\varepsilon^{SO}}$ and ε^{P} were added to the FAS modelling with the aim of collecting the uncertainty on source and path building blocks through the inversion. They act as a proxy and gather contributions from inherent variability and noise, as well as residual contributions due to unmodelled phenomena which depend on the chosen model parametrization for source and path terms. As for the site terms, the total uncertainty $\varepsilon_{SI}(f)$ relative to SRF was calculated from the residual analysis as the geometric standard deviation of the residuals:

$$\varepsilon_{SI,j}\ (f_k) = \sqrt{\frac{\sum_{i=1}^{N_i}\left(\log\frac{\vartheta_{ij}(f_k)}{a_j(f_k)}\right)^2}{N_i}}. \tag{12}$$

This uncertainty gathers contributions related both to the frequency-dependent amplification $a(f)$ and to the frequency-independent inverted parameters (A, κ_0). A first attempt at splitting these contributions by directly inverting the frequency-independent site uncertainty resulted in its strong trade-off with parameter A;

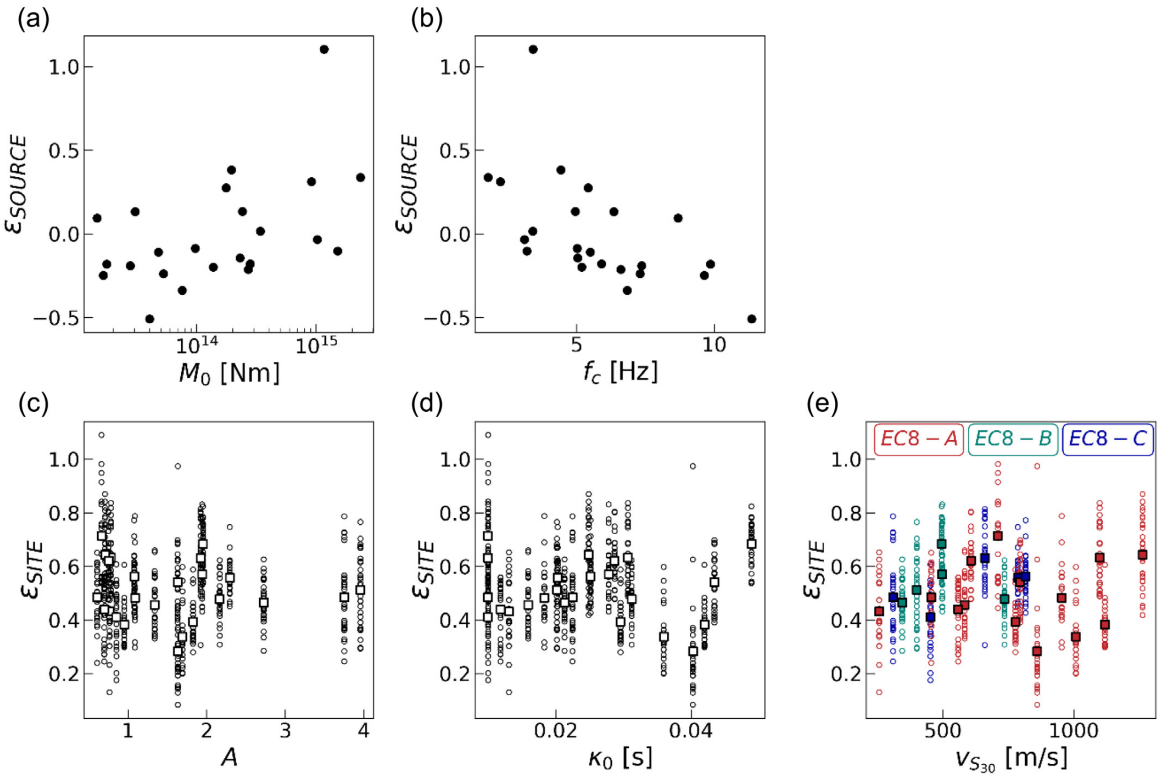

Figure 6. (a) Inverted source uncertainty estimator (ε_{SO}) versus inverted seismic moment M_0, (b) ε_{SO} versus inverted corner frequency, (c) total site uncertainty estimator (ε_{SI}) versus inverted frequency-independent amplification A, (d) ε_{SI} versus inverted station κ_0 and (e) ε_{SI} versus site $v_{s_{30}}$ for sites catalogued as class *EC8-A* (rock; red markers), class *EC8-B* (soil; green markers) and class *EC8-C* (soil; blue markers). For each station, square markers depict the average ε_{SI} over all frequencies.

for this reason, the site uncertainty term was not directly used in the inversion model and the residual analysis method was preferred instead.

Epsilon parameters were checked for correlation and trade-offs with respect to the other inverted quantities; the results are visually reported in Fig. 6. As for the source uncertainty term, we can note a slight positive trend with the uncertainty growing for stronger events. This weak dependency is likely related to the simple, point-source model used to describe the seismic event, suggesting that a different model parametrization should be preferred if the data set were to contain higher magnitude events. As for the site uncertainty term, it shows no evident trade-off with the site amplification parameters A and κ_0, nor with the soil classification in terms of $v_{s_{30}}$ velocity.

As a working hypothesis, we assume that epsilon terms can be combined through uncertainty propagation to obtain an estimate of the standard deviation $\sigma_{\log}$ of the supposedly normally distributed log FAS values, as:

$$\sigma_{\log}(f) = \sqrt{\varepsilon_{SO}^2 + \varepsilon_P^2 + \varepsilon_{SI}^2(f)}. \tag{13}$$

Consequently, the estimate for the mean log FAS spectrum ($\mu_{\log}$) is taken as the modelled spectrum plus the frequency-dependent amplification:

$$\boldsymbol{p}^{\boldsymbol{OUT}} = [\log \boldsymbol{M}_0^{\boldsymbol{OUT}},\ \boldsymbol{f}_c^{\boldsymbol{OUT}},\ Q_0^{OUT},\ \log \boldsymbol{A}^{\boldsymbol{OUT}},\ \boldsymbol{\kappa}^{\boldsymbol{OUT}},\ \boldsymbol{\varepsilon_{SO}} = 0, \varepsilon_P = 0]\ ; \tag{14}$$

$$\mu_{\log} = \log \mathrm{FAS}\left[\boldsymbol{p}^{\boldsymbol{OUT}}\right] + \log a(f). \tag{15}$$

The associated Fourier spectra, which in turn are assumed to have a lognormal distribution, can be obtained in the form of the geometric mean μ^* with associated geometric standard deviation σ^*, as:

$$\mu^* = e^{\mu_{\log}}\ ; \tag{16}$$

$$\sigma^* = e^{\sigma_{\log}}. \tag{17}$$

σ^* was used to define the uncertainty associated to μ^*, with the interval $[\mu^*/\sigma^*, \mu^* \cdot \sigma^*]$ containing 2/3 and the interval $[\mu^*/(\sigma^*)^2, \mu^* \cdot (\sigma^*)^2]$ corresponding to 95 per cent of the probability.

6 RESULTS

6.1 Source parameters

Table 3 lists the source parameters obtained for the 23 events analysed in this study. Inverted seismic moments range between 1.46×10^{13} and 2.35×10^{15} N·m and corner frequencies range between 1.78 and 11.35 Hz. Inverted values are comparable with available seismic moment estimates from literature. For example, $M_0 = 1.52 \times 10^{15}$ N · m was obtained for the 2012 Pordenone event (no. 1 in Table 1), in good agreement with the solution provided by Istituto Nazionale di Geofisica e Vulcanologia (INGV) of $M_0 = 1.03 \times 10^{15}$ N · m.

Direct comparison of M_L magnitudes is not feasible, so M_W values are compared instead. Observed M_L is converted to a 'database' M_W value by using eq. (7), while estimated moment magnitude is calculated from inverted seismic moments using the relationships described in eq. (6). M_W values are well reconstructed for the whole

Table 3. Source parameters of the analysed events. Reference values are taken from the reviewed ISC bulletin (International Seismological Centre 2020) for M_W and from the webservice of Istituto Nazionale di Geofisica e Vulcanologia (INGV; http://terremoti.ingv.it/) for M_0, along with the source classification (SS = strike-slip faulting, TF = thrust faulting and NF = normal faulting). A visual depiction of the results is presented in Fig. 7.

Event	Focal mech.	M_L	M_W	Inverted M_W	M_0 [N · m]	Inverted M_0 [N · m]	Inverted f_c [Hz]	Inverted $\Delta\sigma$ [MPa]
1	TF	4.40	4.08	4.05	1.03E+15	1.52E+15	3.19	9.75
2	TF	3.70	3.62	3.56	1.05E+14	2.80E+14	5.90	11.38
3	n.d.	3.00	3.15	3.08	n.d.	5.27E+13	7.30	4.05
4	n.d.	3.20	3.28	3.19	n.d.	7.56E+13	6.83	4.76
5	SS	4.50	4.15	3.98	1.08E+16	1.16E+15	3.41	9.13
6	SS	3.30	3.35	3.46	1.66E+14	1.95E+14	4.43	3.35
7	TF	4.20	3.95	3.94	5.6E+14	1.02E+15	3.11	6.05
8	n.d.	3.50	3.48	3.52	n.d.	2.41E+14	4.95	5.80
9	TF	3.60	3.55	3.51	1.24E+14	2.30E+14	5.04	5.83
10	n.d.	2.60	2.88	2.92	n.d.	3.04E+13	6.35	1.54
11	NF	3.70	3.62	3.62	1.32E+14	3.40E+14	3.40	2.65
12	SS	4.00	3.82	3.91	1.14E+15	9.12E+14	2.23	2.00
13	TF	4.40	4.08	4.18	5.91E+15	2.35E+15	1.79	2.65
14	n.d.	3.20	3.28	3.26	n.d.	9.70E+13	5.02	2.43
15	n.d.	2.70	2.95	2.89	n.d.	2.77E+13	7.37	2.19
16	TF	3.30	3.35	3.43	1.54E+14	1.76E+14	5.42	5.51
17	n.d.	3.40	3.42	3.36	n.d.	1.37E+14	5.18	3.78
18	n.d.	2.50	2.82	2.76	n.d.	1.76E+13	9.86	3.34
19	n.d.	2.90	3.08	3.05	n.d.	4.76E+13	5.49	1.56
20	n.d.	2.30	2.68	2.71	n.d.	1.46E+13	8.69	1.90
21	n.d.	3.70	3.62	3.56	n.d.	2.71E+14	6.60	15.40
22	n.d.	3.00	3.15	3.00	n.d.	4.02E+13	11.35	11.61
23	n.d.	2.50	2.82	2.74	n.d.	1.65E+13	9.63	2.91

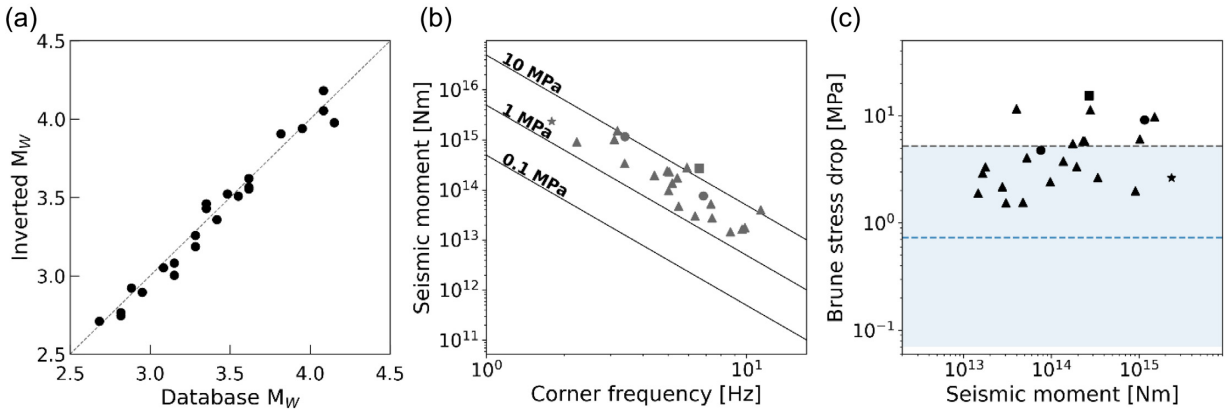

Figure 7. (a) Comparison of inverted M_W with values obtained from database using eq. (7) (black circles). (b) Inverted seismic moment versus corner frequency (grey markers); lines of constant Brune stress drop, computed with eq. (8), are also shown (black lines). (c) Inverted Brune stress drop versus seismic moment (black markers) and related average value (dashed grey line). The range of values obtained by Franceschina *et al.* (2006) for the Friuli Venezia Giulia region is shown for comparison (light blue area), together with its average value (dashed blue line). Circles, triangles and squares represent events occurred in *ZS904*, *ZS905* and *ZS906,* respectively. The star marks event no. 13, occurred outside of *ZS9* zonation.

magnitude range, as the comparison between inverted moment magnitudes and 'database' values shows (Fig. 7a).

Seismic moments are plotted against corner frequencies in Fig. 7(b), together with lines of constant stress drop. Equivalent Brune stress drops $\Delta\sigma$ can be calculated from (Brune 1970):

$$\Delta\sigma = \frac{7}{16} M_0 \left(\frac{f_c}{0.37 v_s} \right)^3 . \quad (18)$$

The stress drop values inferred from inverted parameters are scattered, but mostly lie between 1.5 and 6 MPa, with few values as high as 15.5 MPa (Fig. 7c). If one only considers events occurred inside seismogenic zone *ZS905*, which roughly coincides with the Friuli Venezia Giulia region, most of the stress drop values fall in the range $0.1 - 10$ MPa suggested in the regional study by Franceschina *et al.* (2006, shaded blue area in Fig. 7c). This result is also in line with the global median stress drop for continental collision boundary and transform fault events calculated by Allmann & Shearer (2009). Higher values ($\Delta\sigma \geq 10$ MPa) are found for events occurred in seismic zones *ZS904* and *ZS906* (nos 5 and 21 in Table 1, respectively). This difference could be related to the different seismicity characteristics observed in these zones (cf. Meletti & Valensise 2004), and specifically to the focal mechanism.

6.2 Attenuation parameters

The fall-off of FAS at high frequencies is modelled as deriving from both anelastic attenuation Q and site-related attenuation κ_0. Their combined effect is usually represented through the whole path anelastic attenuation operator, t^* (Anderson & Hough 1984):

$$t^*_{ij} = \frac{r_{ij}}{v_s Q} + \kappa_{0j}, \tag{19}$$

which models spectral decay at high frequencies due to both path and site effects for a simple homogeneous model. In this formulation, κ_0 corresponds to the attenuation effects along the portion of ray paths nearest to the station, whereas Q represents the attenuation effects along ray paths from the source to the station proximity.

The simultaneous estimation of both Q and κ_0 was performed with the awareness of the potential trade-off existing between the two parameters. In order to mitigate it, the geometric spreading function was defined using fixed parameters taken from literature, and a frequency-independent model for Q was preferred. Even so, the results obtained for Q_0 and κ_0 present some issues when compared with independent studies investigating regional seismic wave attenuation.

Console & Rovelli (1981) estimated the quality factor of the Friuli Venezia Giulia region using the strong motion accelerograms of the 1976 earthquake sequence (main shock $M_L = 6.4$), for epicentral distances up to about 200 km. They compared power spectra of entire accelerograms at different distances and obtained the relation $Q(f) = 80 f^{1.1}$, valid for the range $0.1 - 10$ Hz. Malagnini *et al.* (2002) obtained $Q(f) = 260 f^{0.55}$ based on spectral inversion for an area extending from Slovenia to Friuli Venezia Giulia. In comparison, the value of $Q_0 = 1145$ obtained from inversion appears quite higher. It should be stressed, however, that all models proposed by reference literature use a frequency-dependent parametrization of the apparent Q factor, which could partially explain the lower values of Q_0 itself. In fact, when applied to the considered frequency range, the relationship proposed by Malagnini *et al.* (2002) suggests Q factor values between 180 and 1530. Discrepancies in data-selection criteria and in the covered regional area and range of hypocentral distances could also contribute to this difference, as well as different modelling choices.

As for the site attenuation factor, the average value $\kappa_0 = 0.025$ s obtained from inversion is slightly lower than values reported in literature by Gentili & Franceschina (2011, $\kappa_0 = 0.037$ s) and Malagnini *et al.* (2002, $\kappa_0 = 0.045$ s). This can be due to the use of a constant Q model, which is expected to give lower κ_0 values than those obtained using a frequency-dependent Q (Bora *et al.* 2017). The actual range spanned by inverted κ_0 values is $0.01 - 0.05$ s and is compatible with the range of $0.019 - 0.053$ s reported in literature.

Overall, results for individual attenuation parameters obtained from direct inversion are in line with literature values. Different modelling choices could be explored to characterize them, provided that trade-off effects are correctly taken into consideration. For example, following the approach used by Bora *et al.* (2017), the anelastic operator t^* could be used in the model and the attenuation parameters could be subsequently extracted after inversion.

6.3 Site response functions

For each site, the frequency-dependent amplification was computed frequency-wise as the geometric mean of factorial residuals, following the methodology described in Section 5.3. The initial choice of using only stations with at least five associated recordings mitigates the aleatory variability captured by the estimation. This minimum requirement was ensured to also hold for each used frequency. Since spectra were calculated on a different number of frequency values, with upper and lower bounds dictated by SNR, site amplification was calculated only for frequency points with at least five associated FAS values. All amplifications are relative to the average regional *EC8-A* site, defined as the generic rock reference. Site amplification curves provide an estimate of the true site amplification due to upper soil layering beneath the station. It should be kept in mind that the robustness of site amplification estimates still depends on the number of available recordings at each site.

Resultant SRFs, which are obtained from combining the inverted constant amplitude correction A with the frequency-dependent response function $a(f)$ and the site anelastic attenuation κ_0 (cf. eq. 11), are plotted in Fig. 8 for all available stations together with associated error bars of one standard deviation.

Overall, site effects derived from parametric inversion are comparable with values reported in literature. The frequency values corresponding to the main amplification peak for stations FLP and STOL, which are located on alluvium and fluvial sediments, are in good agreement with values reported in ITACA, even if systematically slightly higher (9 Hz versus 8.5 Hz for FLP and3.9 Hz versus 3.7 Hz for STOL). A more thorough comparison is available for station CARC, which has been accurately characterized by Fitzko *et al.* (2007). It is located in the old city centre of Trieste (NE Italy), in the basement of a three-story historical building. The site is on a former salt pan, with a 27 m thick sedimentary cover composed by almost plane layers of clay and silts. Fitzko *et al.* (2007) compared multiple methodologies, namely noise (HVNSR) and earthquake horizontal-to-vertical spectral ratios (HVSR), together with spectral ratios with respect to a reference station. They used standard spectral ratio to retrieve the transfer function of CARC related to the nearby bedrock reference site TRI (MN network) for frequencies up to 8 Hz. There is a good agreement of all results at low frequencies, with a strong amplification around 2 Hz due to the sedimentary structure, followed by another peak around 5.5 Hz (Fig. 9). In particular, the frequency-dependent amplification alone ($a(f)$) correctly matches the shape of HVSR curves but displays a lower amplitude, as a result of not accounting for specific reference conditions. On the other hand, the total site amplification given by the SRF includes the scaling related to the average regional rock site and thus provides values compatible with SSR curves, which are by definition scaled to a reference rock condition (Fig. 9b).

Based on this preliminary comparison of the resulting SRFs with available literature, we are optimistic that the site amplifications obtained using this methodology could be applied for further use, for example, to identify a new regional reference set or to be integrated into site-specific seismic hazard assessment. Knowing that the investigated problem is highly nonlinear and the used methodology is known to be prone to trade-offs between parameters, with the possible consequent introduction of artificial trends, future work will be dedicated to a more accurate validation of the SRFs against other standard approaches.

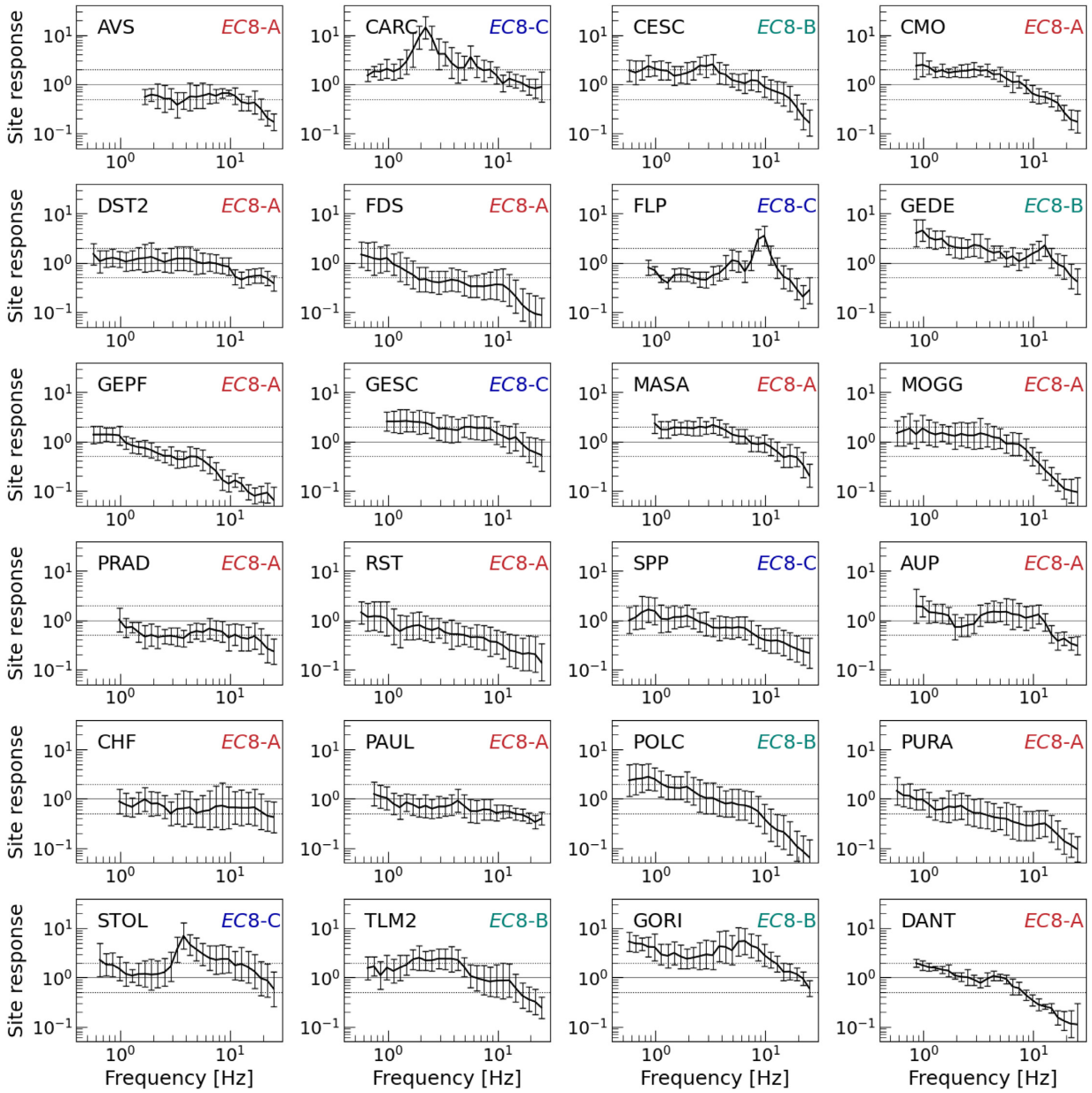

Figure 8. SRFs for the stations used in this work (cf. Table 2). Error bars are 1σ confidence levels; dashed horizontal lines mark the range of amplification values for which the function is considered as flat (amplification between 0.5 and 2).

7 COMPARISON WITH MODEL WITHOUT UNCERTAINTY PARAMETERS

The addition of the epsilon terms in the functional form was tested against the parametrization without the dedicated uncertainty parameters to evaluate how this modelling strategy would affect the inversion results. To do so, a second, independent inversion was performed with same settings as the previous one (in terms of data set, constraints and boundary conditions), with the only exception of the epsilon parameters set to zero. A selection of inverted spectra is depicted in Fig. 10, together with the reference model obtained by including uncertainty terms in the parametrization. All modelled spectra are compatible with the σ^* uncertainty range associated to the results obtained using the uncertainty terms.

The resulting source parameters are reported in Table 4, together with those previously obtained with the parametrization that uses epsilon terms. Both models are equally capable of reproducing the database magnitude and seismic moment values. Corner frequency values are also in good agreement, whereas the calculated stress drop is mostly comparable but slightly higher for high magnitude events in the case with uncertainty modelling.

As for site parameters, a visual comparison of SRFs is presented in Fig. 11. Even if individual parameters vary between the two inversion strategies as an effect of the additional epsilon parameters, the results are in good agreement when the total site response is considered. Moreover, the parametrization that includes the uncertainty terms has the advantage of also providing an uncertainty estimation dedicated to the site response.

Table 4. Source parameters of the analysed events obtained with (ε) or without (no ε) uncertainty modelling. Reference values are derived from the reviewed ISC bulletin (International Seismological Centre 2020) for M_W and from the webservice of INGV (http://terremoti.ingv.it/) for M_0. These results are also graphically represented in Appendix A for visual evaluation.

Event	Database M_W	M_W (ε)	M_W (no ε)	f_c [Hz] (ε)	f_c [Hz] (no ε)	Database M_0 [N · m]	M_0 [N · m] (ε)	M_0 [N · m] (no ε)	$\Delta\sigma$ [MPa] (ε)	$\Delta\sigma$ [MPa] (no ε)
1	4.08	4.05	4.03	3.19	3.19	1.03E+15	1.52E+15	1.38E+15	9.75	8.88
2	3.62	3.56	3.52	5.90	5.91	1.05E+14	2.80E+14	2.36E+14	11.38	9.60
3	3.15	3.08	3.02	7.30	7.29	n.d.	5.27E+13	4.19E+13	4.05	3.21
4	3.28	3.19	3.09	6.83	6.81	n.d.	7.56E+13	5.46E+13	4.76	3.40
5	4.15	3.98	4.30	3.41	3.41	1.08E+16	1.16E+15	3.54E+15	9.13	27.80
6	3.35	3.46	3.57	4.43	4.43	1.66E+14	1.95E+14	2.89E+14	3.35	4.96
7	3.95	3.94	3.93	3.11	3.11	5.6E+14	1.02E+15	9.98E+14	6.05	5.90
8	3.48	3.52	3.56	4.95	4.96	n.d.	2.41E+14	2.78E+14	5.80	6.70
9	3.55	3.51	3.47	5.04	5.04	1.24E+14	2.30E+14	2.01E+14	5.83	5.10
10	2.88	2.92	2.96	6.35	6.35	n.d.	3.04E+13	3.50E+13	1.54	1.77
11	3.62	3.62	3.63	3.40	3.40	1.32E+14	3.40E+14	3.49E+14	2.65	2.72
12	3.82	3.91	4.00	2.23	2.23	1.14E+15	9.12E+14	1.26E+15	2.00	2.75
13	4.08	4.18	4.28	1.79	1.79	5.91E+15	2.35E+15	3.33E+15	2.65	3.75
14	3.28	3.26	3.24	5.02	5.02	n.d.	9.70E+13	8.98E+13	2.43	2.25
15	2.95	2.89	2.84	7.37	7.38	n.d.	2.77E+13	2.31E+13	2.19	1.83
16	3.35	3.43	3.51	5.42	5.42	1.54E+14	1.76E+14	2.33E+14	5.51	7.33
17	3.42	3.36	3.30	5.18	5.18	n.d.	1.37E+14	1.14E+14	3.78	3.13
18	2.82	2.76	2.71	9.86	9.85	n.d.	1.76E+13	1.49E+13	3.34	2.81
19	3.08	3.05	3.02	5.49	5.49	n.d.	4.76E+13	4.30E+13	1.56	1.41
20	2.68	2.71	2.74	8.69	8.68	n.d.	1.46E+13	1.62E+13	1.90	2.10
21	3.62	3.56	3.50	6.60	6.61	n.d.	2.71E+14	2.21E+14	15.40	12.60
22	3.15	3.00	2.86	11.35	11.44	n.d.	4.02E+13	2.42E+13	11.61	7.18
23	2.82	2.74	2.68	9.63	9.62	n.d.	1.65E+13	1.30E+13	2.91	2.29

Overall, the comparison shows that the inclusion of uncertainty parameters in the functional form does not bias the inversion capability with respect to a simpler parametrization. Conversely, it allows the algorithm to accommodate the epistemic uncertainty related to the different model component (source, path and site). In fact, the concept behind the use of epsilon terms is that of using them as an indicator of how much different FAS models could reduce epistemic uncertainty. Their values should not be used *per se* but compared between inversion runs featuring different parametrization choices.

8 CONCLUSIONS

We developed a flexible strategy to solve the parametric inversion problem related to FAS modelling. The procedure relies on conventional decomposition of the FAS into source, propagation and site response contributions, with the addition of uncertainty collectors. These terms were evaluated through a parametric approach by a single-step recursive quasi-Newton inversion in the frequency band $0.5 - 25.0$ Hz. The methodology was applied on a data set of 234 velocity FAS corresponding to 23 events recorded by 24 stations located in northeast Italy, at the boundary with Slovenia and Austria.

It should be kept in mind that all the obtained results are relative to the region-specific parametric model. As for source parameters, the underlying assumption is that a Brune source model with a single corner frequency and an f^2 fall-off can realistically describe small earthquakes such as those composing the data set. In this regard, obtained M_W values are observed to scale with M_L with a slope slightly lower than 1.5 (cf. Deichmann 2006), as expected and already observed for other regions for low to moderate events (e.g. Drouet *et al.* 2008). As for attenuation parameters, the simple model based on frequency-independent Q_0 and κ_0 parameters was purposedly adopted to avoid introducing further error sources, also considering that the model itself is less sensitive to their variation with respect to source parameters. The well-known trade-off between source parameters and geometrical spreading was minimized by constraining the latter *a priori* based on literature; nonetheless, a complementary modelling configuration could also be tested, by directly inverting the spreading function while bounding source seismic moment variability.

Site response curves relative to network average rock condition were reconstructed by combining inverted amplification parameters together with information extracted from residual analysis. Site-specific amplification factors as high as 10 were found, with typical resonance frequencies in the range $2 - 9$ Hz. The retrieved amplification curves were visually compared with those reported in other studies using different methodologies, such as SSR and HVSR, and are found to be capable of correctly characterizing both the frequency value and the amplitude of the main amplification peaks. However, a dedicated work is necessary to further validate these results and to discuss the amplification properties of each station, together with its geological characterization.

Finally, we discussed the introduction of uncertainty estimators directly into the spectral model. The comparison with results obtained without such estimators showed that a small difference in the assumptions leads to a model that fits the data compatibly with the associated uncertainty. We find this an encouraging result concerning the possibility of using the uncertainty estimators as a benchmark to compare different modelling hypotheses. More importantly, their application might be investigated for the use with stochastic ground motion simulations. We are confident that including additional data will improve the statistics and allow us to gain further insight on the models' uncertainties. As Edwards *et al.* (2008) underlined, however, each resulting model must be treated as an interdependent set, in order not to break down the covariance that holds it together. This assumption allows us to extract useful seismological information from weak-motion regional data sets

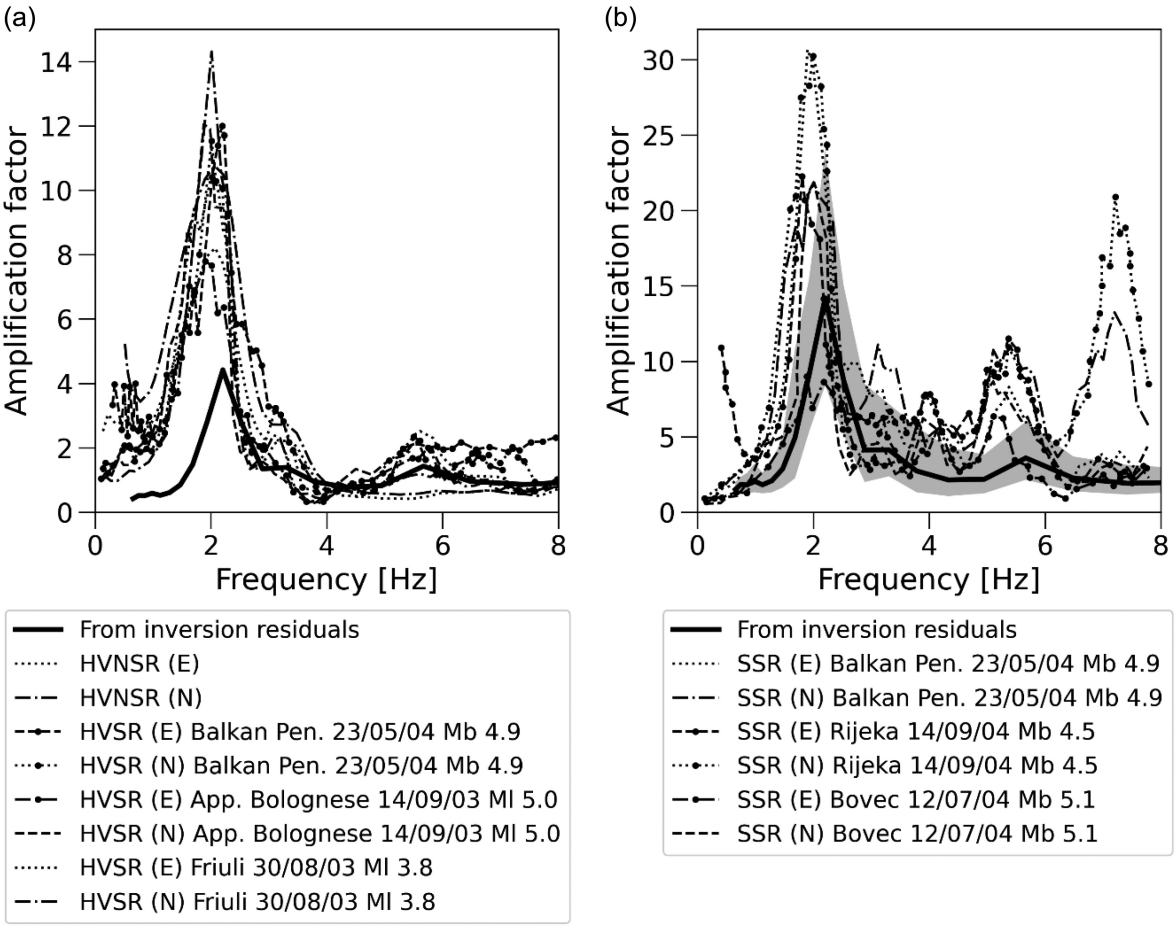

Figure 9. Site amplification determined from spectral inversion for station CARC (solid black line) for frequency-dependent amplification (a) and for total response function (b), compared with results obtained by Fitzko *et al.* (2007) using HVNSR, HVSR and SSR methods (dashed and dotted lines). The shaded grey area represents the 1σ uncertainty range.

and to safely use it, provided that more constraints are applied in extrapolating the results to higher magnitudes.

Remaining known limitations are the propagation of errors between inversion steps and the possible overestimation of ground motion amplitude for larger magnitude events. The former issue was mitigated by keeping a simple methodology workflow to simultaneously invert for most of the parameters. The latter arises from the fact that we do not consider the effects of nonlinear soil behaviour due to larger magnitude earthquakes. However, as the maximum expected magnitude for the investigated area is around $M_W = 6$, this could become an issue only for strong shaking levels at very short source-to-site distances (Edwards *et al.* 2008).

The results obtained in this study outline the capability of regional spectral parametric inversion to realistically model FAS, even when simple modelling choices are used. The retrieval of site amplification curves through the application of analysis residuals provides an advisable solution for the analysis of data from any regional network, with possible applications in seismic monitoring and engineering seismology. Future studies will be focused on systematically validating site amplification results against those obtained from other standard approaches. Future work will also be dedicated to introducing and evaluating further modelling complexities, upon the inclusion of additional data. To do so, we plan to introduce a time-dependent, spatially extended representation of the source model, as well as a whole path anelastic attenuation operator t^* (cf. Bora *et al.* 2017). This will possibly increase the model capability of describing epistemic uncertainty and lead to a better resolution of the extracted seismological information.

ACKNOWLEDGMENTS

The authors wish to express their grateful thanks to the SeisRaM group of the Department of Mathematics and Geosciences (University of Trieste) for the waveform data used in this study. This work greatly benefitted from the useful suggestions and insights by Dr Sreeram R. Kotha (ISTerre Grenoble) and by another anonymous Reviewer.

LC was affiliated with the SeisRaM group at University of Trieste during the majority of the research work and is currently affiliated with Istituto Nazionale di Oceanografia e di Geofisica Sperimentale (OGS).

This work was co-funded by the Italian Department of Civil Protection—Presidency of the Council of Ministers through the grant no. 1541/20 of the University of Trieste.

All authors contributed to the study conception and design. Material preparation, data collection and analysis were performed by LC, with the support of all other authors. Manuscript writing was carried out by LC. All authors commented on previous versions of the manuscript. All authors read and approved the final manuscript.

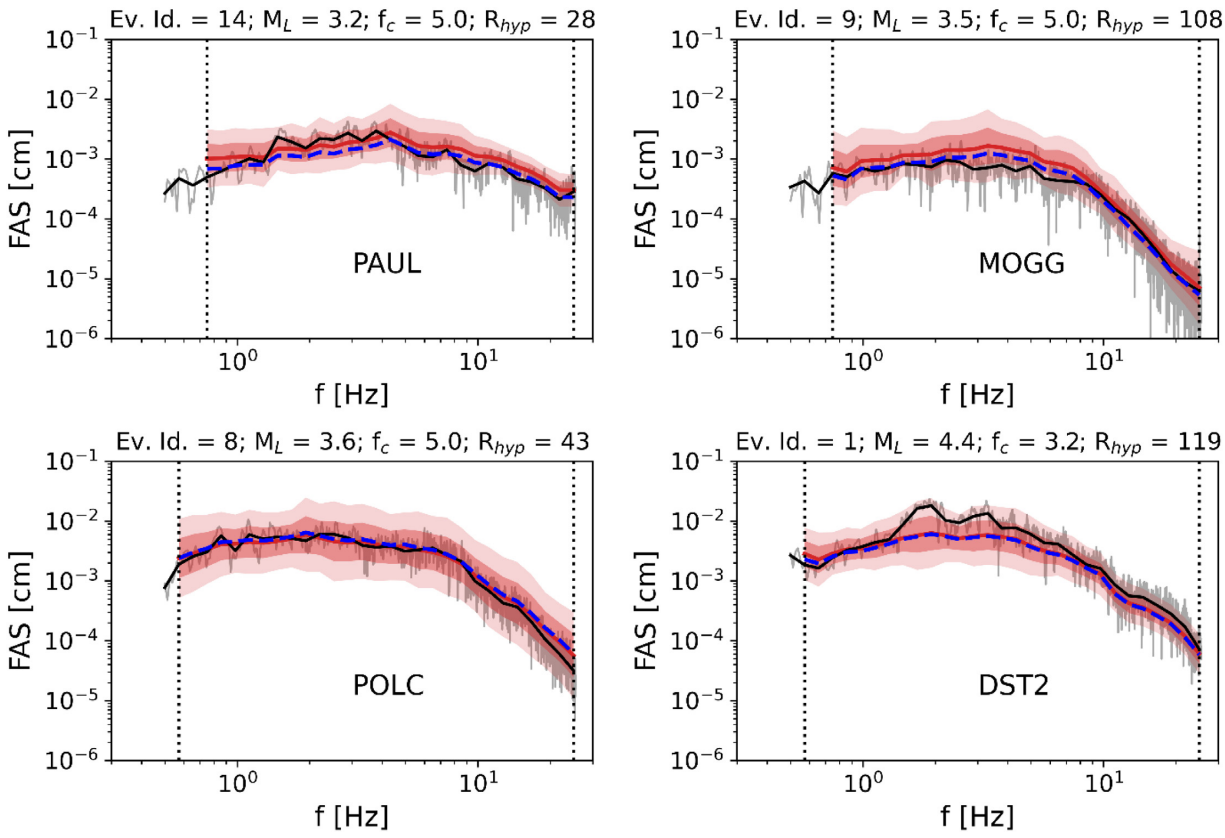

Figure 10. Example of modelled spectral curves for the observed velocity FAS (grey lines) obtained when the uncertainty terms are included in the model used for inversion (red lines) and when they are excluded (blue dashed lines). The associated uncertainty bands obtained for the first case are shown as shaded red areas, corresponding to 66 per cent (dark red) and 95 per cent probability (light red), respectively. Inversion was performed on the smoothed version of the spectra (black lines), using spectral amplitudes inside the usable frequency range (vertical dotted lines).

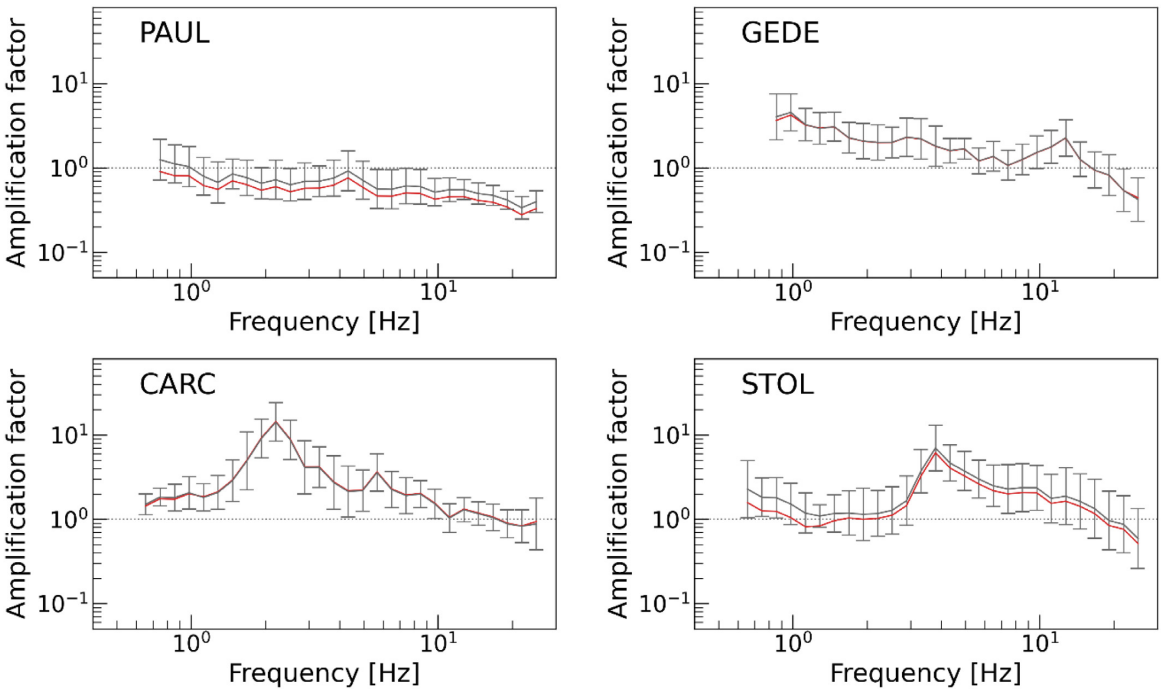

Figure 11. Total SRFs for stations PAUL (*EC8-A*), GEDE (*EC8-B*), CARC and STOL (*EC8-C*). Grey and red lines are results obtained from the parametric model including (ε) and excluding (no ε) uncertainty terms, respectively. Error bars are 1σ confidence levels on the mean response functions, calculated using the uncertainty terms.

DATA AVAILABILITY AND RESOURCES

The data underlying this article were accessed from different sources in the public domain.

Parametric information on the events was accessed from the International Seismological Centre (2020) On-line Bulletin, https://doi.org/10.31905/D808B830. Associated information on source seismic moment was taken from the webservice of Istituto Nazionale di Geofisica e Vulcanologia (http://terremoti.ingv.it/)

Waveforms are available upon request from the Central Eastern Europe Earthquake Research Network http://www.ce3rn.eu/. The networks interrogated for this work were:

(i) [code IT] Presidency of Council of Ministers—Civil Protection Department. (1972). Italian Strong Motion Network [Data set]. International Federation of Digital Seismograph Networks. https://doi.org/10.7914/SN/IT

(ii) [code NI] OGS (Istituto Nazionale di Oceanografia e di Geofisica Sperimentale) and University of Trieste. (2002). North-East Italy Broadband Network [Data set]. International Federation of Digital Seismograph Networks. https://doi.org/10.7914/SN/NI

(iii) [code OE] ZAMG—Zentralanstalt für Meterologie und Geodynamik. (1987). Austrian Seismic Network [Data set]. International Federation of Digital Seismograph Networks. https://doi.org/10.7914/SN/OE

(iv) [code OX] Istituto Nazionale di Oceanografia e di Geofisica Sperimentale—OGS. (2016). North-East Italy Seismic Network [Data set]. FDSN. https://doi.org/10.7914/SN/OX

(v) [code RF] University of Trieste. (1993). Friuli Venezia Giulia Accelerometric Network [Data set]. International Federation of Digital Seismograph Networks. https://doi.org/10.7914/SN/RF

(vi) [code SL] Slovenian Environment Agency. (1990). Seismic Network of the Republic of Slovenia [Data set]. International Federation of Digital Seismograph Networks. https://doi.org/10.7914/SN/SL

The derived data generated in this research will be shared on reasonable request to the corresponding author. The software used to perform spectral inversion will be released inside the ShakeLab Python opensource project https://github.com/shakelab/shakelab

CONFLICT OF INTEREST

All authors declare that they have no conflict of interest.

REFERENCES

Allmann, B.P. & Shearer, P.M., 2009. Global variations of stress drop for moderate to large earthquakes, *J. geophys. Res.,* **114,** B01310.

Anderson, J.G. & Hough, S.E., 1984. A model for the shape of the Fourier amplitude spectrum of acceleration at high frequencies, *Bull. seism. Soc. Am.,* **74**(5), 1969–1993.

Andrews, D.J., 1986. Objective determination of source parameters and similarity of earthquakes of different size, in *Earthquake Source Mechanics,* Das, S., Boatwright, J. & Scholz, C.H., eds. American Geophysical Union, Washington DC.

Atkinson, G.M. & Boore, D.M., 1995. Ground-motion relations for eastern North America, *Bull. seism. Soc. Am.,* **85**(1), 17–30.

Bindi, D., Parolai, S., Grosser, H., Milkereit, C. & Karakisa, S., 2006. Crustal attenuation characteristics in northwestern Turkey in the range from 1 to 10 Hz, *Bull. seism. Soc. Am.,* **96,** 200–214.

Boatwright, J., 1978. Detailed spectral analysis of two small New York State earthquakes, *Bull. seism. Soc. Am.,* **68,** 1117–1131.

Bommer, J.J. *et al.*, 2017. Framework for a ground-motion model for induced seismic hazard and risk analysis in the Groningen gas field, The Netherlands, *Earthq. Spectra,* **33**(2), 481–498.

Boore, D.M., 1983. Stochastic Simulation of high frequency ground motions based on seismological models of the radiated spectra, *Bull. seism. Soc. Am.,* **73**(6), 1865–1894.

Boore, D.M., 2003. Simulation of ground motion using the stochastic method, *Pure appl. Geophys.,* **160**(3), 635–676.

Boore, D.M. & Boatwright, J., 1984. Average body-wave radiation coefficients, *Bull. seism. Soc. Am.,* **74,** 1615–1621.

Bora, S.S., Scherbaum, F., Kuehn, N., Stafford, P. & Edwards, B., 2015. Development of a response spectral ground-motion prediction equation (GMPE) for seismic-hazard analysis from empirical Fourier spectral and duration models, *Bull. seism. Soc. Am.,* **105**(4), 2192–2218.

Bora, S.S., Cotton, F., Scherbaum, F., Edwards, B. & Traversa, P., 2017. Stochastic source, path and site attenuation parameters and associated variabilities for shallow crustal European earthquakes, *Bull. Earthq. Eng.,* **15,** 4531–4561.

Bragato, P.L., Sugan, M., Augliera, P., Massa, M., Vuan, A. & Saraò, A., 2011. Moho reflection effects in the Po plain (northern Italy) observed from instrumental and intensity data, *Bull. seism. Soc. Am.,* **101**(5), 2142–2152.

Bragato, P.L. *et al.*, 2014. The Central and Eastern European Earthquake Research Network-CE3RN, *Geophys. Res. Abstr.,* **16,** 13911.

Bressan, G., Bragato, P.L. & Venturini, C., 2003. Stress and strain tensors based on focal mechanisms in the seismotectonic framework of the Friuli-Venezia Giulia region (northeastern Italy), *Bull. seism. Soc. Am.,* **93,** 1280–1290.

Brune, J.N., 1970. Tectonic stress and the spectra of seismic shear waves from earthquakes, *J. geophys. Res.,* **75**, 4997–5010.

Brune, J.N., 1971. Correction: tectonic stress and the spectra of seismic shear waves from earthquakes, *J. geophys. Res.,* **76,** 5002.

Castro, R.R., Anderson, J.G. & Singh, S.K., 1990. Site response, attenuation and source spectra of S waves along the Guerrero, Mexico, subduction zone, *Bull. seism. Soc. Am.,* **80,** 1481–1503.

Castro, R.R., Pacor, F. & Petrungaro, C., 1997. Determination of S-wave energy release of earthquakes in the region of Friuli, Italy, *Geophys. J. Int.,* **128,** 399–408.

Castro, R.R., Pacor, F., Sala, A. & Petrungaro, C., 1996. S wave attenuation and site effects in the region of Friuli, Italy, *J. geophys. Res.,* **101**(B10), 22355–22369.

Console, R. & Rovelli, A., 1981. Attenuation parameters for Friuli region from strong-motion accelerogram spectra, *Bull. seism. Soc. Am.,* **71**(6), 1981–1991.

Cotton, F., Scherbaum, F., Bommer, J.J. & Bungum, H., 2006. Criteria for selecting and adjusting ground-motion models for specific target applications: applications to Central Europe and rock sites, *J. Seismol.,* **10,** 137–156.

Cuffaro, M., Riguzzi, F., Scrocca, D., Antonioli, F., Carminati, E., Livani, M. & Doglioni, C., 2010. On the geodynamics of the northern Adriatic plate, *Rend. Fis. Acc. Lincei,* **21**(1), 253–279.

D'Amico, M., Felicetta, C., Russo, E., Sgobba, S., Lanzano, G., Pacor, F. & Luzi, L., 2020. Italian Accelerometric Archive v 3.1—Istituto Nazionale di Geofisica e Vulcanologia, Dipartimento della Protezione Civile Nazionale,

Deichmann, N., 2006. Local magnitude, a moment revisited, *Bull. seism. Soc. Am.,* **96**(4A), 1267–1277.

Drouet, S., Chevrot, S., Cotton, F. & Souriau, A., 2008. Simultaneous inversion of source spectra, attenuation parameters, and site responses: application to the data of the French Accelerometric Network, *Bull. seism. Soc. Am.,* **98,** 198–219.

EC8, 2004. *Eurocode 8: Design of Structures for Earthquake Resistance. Part 1: General Rules, Seismic Actions and Rules for Buildings*. Brussels, Belgium: European Norm, European Committee for Standardisation, European Committee for Standardisation Central Secretariat.

Edwards, B., Rietbrock, A., Bommer, J.J. & Baptie, B., 2008. The acquisition of source, path, and site effects from microearthquake recordings using Q

tomography: application to the United Kingdom, *Bull. seism. Soc. Am.,* **98**(4), 1915–1935.
Edwards, B. & Fäh, D., 2013. Measurements of stress parameter and site attenuation from recordings of moderate to large earthquakes in Europe and the Middle East, *Geophys. J. Int.,* **194**(2), 1190–1202.
Fitzko, F., Costa, G., Delise, A. & Suhadolc, P., 2007. Site effects analyses in the old city center of Trieste (NE Italy) using accelerometric data, *J. Earthq. Eng.,* **11,** 33–48.
Franceschina, G., Kravanja, S. & Bressan, G., 2006. Source parameters and scaling relationships in the Friuli-Venezia Giulia (Northeastern Italy) region, *Phys. Earth Planet. Inter.,* **154**(2), 48–167.
Galadini, F., Poli, M.E. & Zanferrari, A., 2005. Seismogenic sources potentially responsible for earthquakes with M ≥ 6 in the eastern Southern Alps (Thiene-Udine sector, NE Italy), *Geophys. J. Int.,* **161**(3), 739–762.
Gallo, A., Costa, G. & Suhadolc, P., 2014. Near real-time automatic moment magnitude estimation, *Bull. Earthq. Eng.,* **12**, 185–202.
Gentile, G. F., Bressan, G., Burlini, L. & De Franco, R., 2000. Three-dimensional VP and VP/VS models of the upper crust in the Friuli area (northeastern Italy), *Geophys. J. Int.,* **141**(2), 457–478.
Gentili, S. & Franceschina, G., 2011. High frequency attenuation of shear waves in the southeastern Alps and northern Dinarides, *Geophys. J. Int.,* **185**(3), 1393–1416.
Hanks, T.C. & Kanamori, H., 1979. A moment magnitude scale, *J. geophys. Res.,* **84**(B5), 2348–2350.
International Seismological Centre, 2020. On-line Bulletin.
Klin, P., Laurenzano, G., Barnaba, C., Priolo, E. & Parolai, S., 2021. Site amplification at permanent stations in northeastern Italy, *Bull. seism. Soc. Am.,* **111**, 1885–1904.
Konno, K. & Ohmachi, T., 1998. Ground-motion characteristics estimated from spectral ratio between horizontal and vertical components of microtremor, *Bull. seism. Soc. Am.,* **88**(1), 228–241.
Kraft, D., 1988. A software package for sequential quadratic programming (DFVLR-FB 88-28), DLR German Aerospace Center – Institute for Flight Mechanics, Koln, Germany.
Malagnini, L., Akinci, A., Herrmann, R., Pino, N. & Scognamiglio, L., 2002. Characteristics of the ground motion in northeastern Italy, *Bull. seism. Soc. Am.,* **92,** 2186–2204.
Meletti, C. & Valensise, G., 2004. Zonazione sismogenetica ZS9–App. 2 al rapporto conclusivo. Gruppo di Lavoro MPS (2004), Redazione della mappa di pericolosità sismica prevista dall'Ordinanza PCM 3274 (2004). Available at: http://zonesismiche.mi.ingv.it/documenti/App2.pdf
Michel, C., Fäh, D., Edwards, B. & Cauzzi, C., 2017. Site amplification at the city scale in Basel (Switzerland) from geophysical site characterization and spectral modelling of recorded earthquakes, *Phys. Chem. Earth,* **98,** 27–40,
Munafò, I., Malagnini, L. & Chiaraluce, L., 2016. On the relationship between Mw and ML for small earthquakes, *Bull. seism. Soc. Am.,* **106,** 2402–2408.
Oth, A., Bindi, D., Parolai, S. & Wenzel, F., 2008. *S*-wave attenuation characteristics beneath the Vrancea region in Romania: new insights from the inversion of ground-motion spectra, *Bull. seism. Soc. Am.,* **98**(5), 2482–2497.
Oth, A., Bindi, D., Parolai, S. & Di Giacomo, D., 2011. Spectral analysis of K-NET and KiK-net Data in Japan, Part II: on attenuation characteristics, source spectra, and site response of borehole and surface stations, *Bull. seism. Soc. Am.,* **101**(2), 667–687.
Pacor, F. *et al.*, 2016. Spectral models for ground motion prediction in the L'Aquila region (central Italy): evidence for stress-drop dependence on magnitude and depth, *Geophys. J. Int.,* **204**(2), 697–718.
Parolai, S., Bindi, D. & Augliera, P., 2000. Application of the generalized inversion technique (GIT) to a microzonation study: numerical simulations and comparison with different site-estimation techniques, *Bull. seism. Soc. Am.,* **90,** 286–297.
Parolai, S., Bindi, D., Baumbach, M., Grosser, H., Milkereit, C., Karakisa, S. & Zunbul, S., 2004. Comparison of different site response estimation techniques using aftershocks of the 1999 Izmit earthquake, *Bull. seism. Soc. Am.,* **94,** 1096.
Poggi, V., Edwards, B. & Fäh, D., 2011. Derivation of a reference shear-wave velocity model from empirical site amplification, *Bull. seism. Soc. Am.,* **101**(1), 258–274.
Rietbrock, A., Strasser, F. & Edwards, B., 2013. A stochastic earthquake ground-motion prediction model for the United Kingdom, *Bull. seism. Soc. Am.,* **103**(1), 57–77.
Salazar, W., Sardina, V. & de Cortina, J., 2007. A hybrid inversion technique for the evaluation of source, path, and site effects employing S-wave spectra for subduction and upper-crustal earthquakes in El Salvador, *Bull. seism. Soc. Am.,* **97**, 208–221.
Scherbaum, F., 1990. Combined inversion for the three-dimensional Q structure and source parameters using microearthquake spectra, *J. geophys. Res.,* **95**(B8), 12423–12438.
Scherbaum, F., Bommer, J.J., Bungum, H., Cotton, F. & Abrahamson, N.A., 2005. Composite ground-motion models and logic trees: methodology, sensitivities and uncertainties, *Bull. seism. Soc. Am.,* **95**, 1575–1593.
Sugan, M. & Vuan, A., 2014. On the ability of Moho reflections to affect the ground motion in northeastern Italy: a case study of the 2012 Emilia seismic sequence, *Bull. Earthq. Eng.,* **12,** 2179–2194.
Wald, D.J. & Allen, T.I., 2007. Topographic slope as a proxy for seismic site conditions and amplification, *Bull. seism. Soc. Am.,* **97**(5), 1379–1395.
Zollo, A., Orefice, A. & Convertito, V., 2014. Source parameter scaling and radiation efficiency of microearthquakes along the Irpinia Fault Zone in Southern Apennines, Italy, *J. geophys. Res.—Solid Earth,* **119,** 3256–3275.

APPENDIX A - COMPARISON OF INVERTED SOURCE PARAMETERS FOR DIFFERENT UNCERTAINTY MODELLING CHOICES

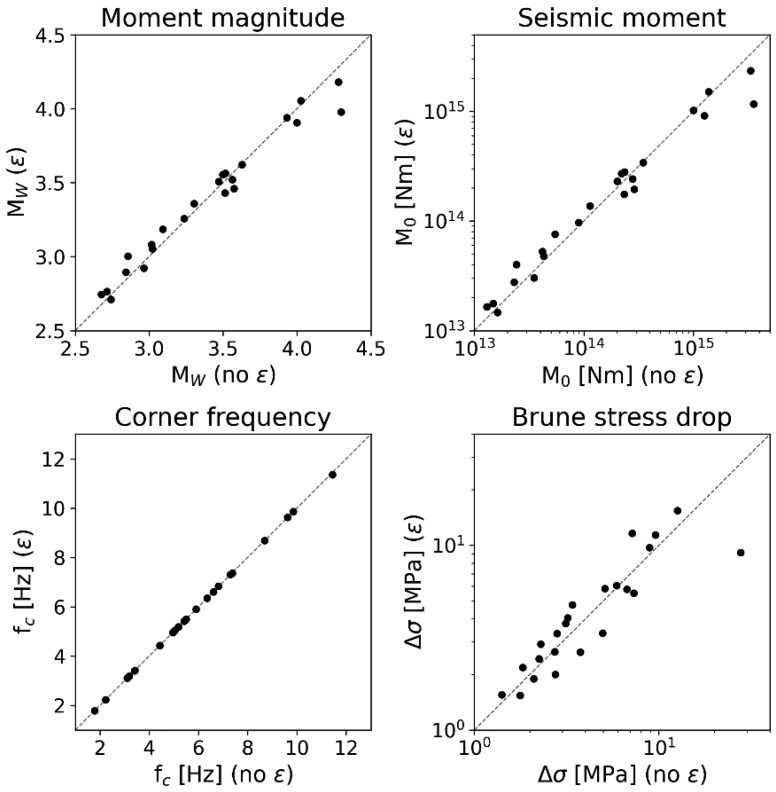

Figure A1. Source parameters of the analysed events obtained with (ε) or without (no ε) uncertainty modelling, as described in Section 7; (a) moment magnitude, (b) inverted seismic moment, (c) inverted corner frequency and (d) stress drop.